The African monsoon during the early Eocene from the DeepMIP simulations

Charles Williams[1], Daniel J. Lunt[1], Ulrich Salzmann[2], Tammo Reichgelt[3], Gordon N. Inglis[4], David R Greenwood[5], Wing-Le Chan[6], Ayako Abe-Ouchi[6], Yannick Donnadieu[7], David Hutchinson[8], Agatha Margaretha De Boer[9], Jean-Baptiste Ladant[10], Polina A Morozova[11], Igor Niezgodzki[12], Gregor Knorr[13], Sebastian Steinig[1], Zhang Zhong-Shi[14], Jiang Zhu[15], Matthew Huber[16], and Bette L Otto-Bliesner[17]

[1]University of Bristol
[2]Northumbria University
[3]University of Connecticut
[4]University of Southampton
[5]Brandon University
[6]University of Tokyo
[7]CEREGE (Centre Européen de Recherche et d'Enseignement des Géosciences de l'Environnement)
[8]University of New South Wales
[9]Stockholm University
[10]Laboratoire des Sciences du Climat et de l'Environnement
[11]Institute of Geography, Russian Academy of Sciences
[12]Institute of Geological Sciences PAN
[13]AWI Bremerhaven
[14]Bjerknes Centre for Climate Research
[15]National Center for Atmospheric Research
[16]Purdue University
[17]National Center for Atmospheric Research (UCAR)

November 24, 2022

Abstract

The early Eocene (~56-48 million years ago) is characterised by high CO_2 estimates (1200-2500 ppmv) and elevated global temperatures (~10 to 16°C higher than modern). However, the response of the hydrological cycle during the early Eocene is poorly constrained, especially in regions with sparse data coverage (e.g. Africa). Here we present a study of African hydroclimate during the early Eocene, as simulated by an ensemble of state-of-the-art climate models in the Deep-time Model Intercomparison Project (DeepMIP). A comparison between the DeepMIP pre-industrial simulations and modern observations suggests that model biases are model- and geographically dependent, however these biases are reduced in the model ensemble mean. A comparison between the Eocene simulations and the pre-industrial suggests that there is no obvious wetting or drying trend as the CO_2 increases. The results suggest that changes to the land sea mask (relative to modern) in the models may be responsible for the simulated increases in precipitation to the north of Eocene Africa, whereas it is likely that changes in vegetation in the models are responsible for the simulated region of drying over equatorial Eocene Africa. There is an increase in precipitation over equatorial and West Africa and associated drying over northern Africa as CO_2 rises. There are also important dynamical

1

changes, with evidence that anticyclonic low-level circulation is replaced by increased south-westerly flow at high CO_2 levels. Lastly, a model-data comparison using newly-compiled quantitative climate estimates from palaeobotanical proxy data suggests a marginally better fit with the reconstructions at lower levels of CO2.

The African monsoon during the early Eocene from the DeepMIP simulations

Charles J. R. Williams[1,2], Daniel J. Lunt[1], Ulrich Salzmann[3], Tammo Reichgelt[4], Gordon N. Inglis[5], David R. Greenwood[6], Wing-Le Chan[7], Ayako Abe-Ouchi[7], Yannick Donnadieu[8], David K. Hutchinson[9,10], Agatha M. de Boer[9], Jean-Baptiste Ladant[11], Polina A. Morozova[12], Igor Niezgodzki[13,14], Gregor Knorr[14], Sebastian Steinig[1], Zhongshi Zhang[15], Jiang Zhu[16], Matthew Huber[17], Bette L. Otto-Bliesner[16]

[1]School of Geographical Sciences, University of Bristol, UK

[2]NCAS / Department of Meteorology, University of Reading, UK

[3]Geography and Environmental Sciences, Northumbria University, UK

[4]Department of Geosciences, University of Connecticut, US

[5]School of Ocean and Earth Science, University of Southampton, UK

[6]Department of Biology, Brandon University, Canada

[7]Atmosphere and Ocean Research Institute, The University of Tokyo, Japan

[8]Laboratoire des Sciences du Climat et de l'Environnement, France

[9]Department of Geological Sciences, Stockholm University, Sweden

[10]Climate Change Research Centre, University of New South Wales, Australia

[11]Earth and Environmental Sciences, University of Michigan, US

[12]Institute of Geography, Russian Academy of Sciences, Russia

[13]Institute of Geological Sciences, Polish Academy of Sciences, Poland

[14]Alfred Wegener Institute for Polar and Marine Research, Germany

[15]Bjerknes Centre for Climate Research, University of Bergen, Norway

[16]Climate and Global Dynamics Laboratory, National Center for Atmospheric Research, US

[17]Department of Earth, Atmospheric and Planetary Sciences, Perdue University, US

Corresponding author address: School of Geographical Sciences, University Road, Bristol, BS8 1SS, UK

Email: c.j.r.williams@bristol.ac.uk

Short title: Early Eocene simulations of the African monsoon

KEY POINTS

1) State-of-the-art climate models are used to study African hydroclimate during the early Eocene (approximately 50 million years ago).

2) With increasing levels of CO_2, there are changes to African precipitation, due to dynamical changes such as low level circulation.

3) A comparison between the models and newly-compiled climate estimates shows a marginally better match at lower levels of CO_2.

ABSTRACT

The early Eocene (~56-48 million years ago) is characterised by high CO_2 estimates (1200-2500 ppmv) and elevated global temperatures (~10 to 16°C higher than modern). However, the response of the hydrological cycle during the early Eocene is poorly constrained, especially in regions with sparse data coverage (e.g. Africa). Here we present a study of African hydroclimate during the early Eocene, as simulated by an ensemble of state-of-the-art climate models in the Deep-time Model Intercomparison Project (DeepMIP). A comparison between the DeepMIP pre-industrial simulations and modern observations suggests that model biases are model- and geographically dependent, however these biases are reduced in the model ensemble mean. A comparison between the Eocene simulations and the pre-industrial suggests that there is no obvious wetting or drying trend as the CO_2 increases. The results suggest that changes to the land sea mask (relative to modern) in the models may be responsible for the simulated increases in precipitation to the north of Eocene Africa, whereas it is likely that changes in vegetation in the models are responsible for the simulated region of drying over equatorial Eocene Africa. There is an increase in precipitation over equatorial and West Africa and associated drying over northern Africa as CO_2 rises. There are also important dynamical changes, with evidence that anticyclonic low-level circulation is replaced by increased south-westerly flow at high CO_2 levels. Lastly, a model-data comparison using newly-compiled quantitative climate estimates from palaeobotanical proxy data suggests a marginally better fit with the reconstructions at lower levels of CO2.

1. INTRODUCTION

One of the ways to better understand future anthropogenic-induced climate change is to simulate past climates, using these as partial analogues for the future and allowing the testing of climate models to simulate climates very different from today (Braconnot *et al*. 2011, Tierney *et al*. 2020). Simulating past climates allows not only an interrogation of the mechanisms of past climate change (Haywood *et al*. 2020, Lunt *et al*. 2021), but if a robust comparison with available proxy data can be produced, this allows confidence in future climate change projections that are often based on models tuned to a modern climate state (Harrison *et al*. 2014, Taylor *et al*. 2011, Williams *et al*. 2020, Williams *et al*. 2021, Zhu *et al*. 2020).

It has long been known that African precipitation, and in particular that of the West African monsoon, is of vital importance to the more than one billion people in sub-Saharan Africa who survive predominantly on rain-fed agriculture and, concurrently, are highly vulnerable to extreme precipitation events causing both flooding and drought (Williams and Kniveton 2011). However, a lack of weather and climate data across much of the continent has resulted in a high level of uncertainty concerning both present day and future climate trends (Salerno *et al*. 2019), and although it is expected that both average temperature and precipitation will increase across Africa along with the rest of the world (IPCC 2021), regional variation is particularly high across Africa.

Due to their particular relevance to African monsoon precipitation, two Quaternary time periods have recently been investigated by Williams *et al*. (2020) under the Palaeoclimate Modelling Intercomparison Project (PMIP, Braconnot *et al*. 2007), now in its 4th phase and itself under the umbrella of the Coupled Model Intercomparison Project, now in its 6th phase (CMIP6, Eyring *et al*. 2016). These time periods are the mid-Holocene (6000 years ago, 6 ka) and Last Interglacial (127 ka). However, excess warmth and enhancement of Northern Hemisphere monsoons during these periods is caused primarily by changes to the orbital configuration of Earth, rather than elevated greenhouse gases (Kageyama *et al*. 2018). To investigate substantial greenhouse gas-induced warming, and its result on monsoon systems such as across Africa, periods further back in time are needed, and two such candidates in the context of PMIP are the mid-Pliocene (~3 million years ago, 3 Ma) and the early Eocene (~56.05-47.8 Ma, hereafter referred to as the Eocene). However, with CO_2 levels ranging from 316-420 ppmv during the mid-Pliocene (Martínez-Botí *et al*. 2015), this is more similar to modern levels rather than being a suitable analogue for future projections by the end of the 21st century; using the previous RCP 8.5 scenario, this could be over 1000 ppmv (IPCC 2013). The Eocene, with CO_2 levels ranging between 1200-2500 ppmv (Anagnostou *et al*. 2016, Anagnostou *et al*. 2020, Lunt *et al*. 2021), is comparable to the current future projections, and in particular for the extended high-emissions scenarios such as in the year 2300 under SSP5-8.5 (Arias *et al*. 2021). As a result of this high CO_2, the early Eocene was a period characterised by temperatures ~5°C higher than

101   today in the tropics (e.g., Inglis *et al*,.2020 Pearson *et al*. 2007), and much greater polar amplification

102   with temperatures reaching ~20°C warmer than today at terrestrial high latitudes (e.g. Huber and

103   Caballero 2011, Naafs *et al*. 2018, van Dijk *et al*. 2020).

104

105   Despite being a partial analogue for future climate change, until the last few years climate model

106   simulations of high CO_2 periods such as the Eocene have not been evaluated within a consistent

107   framework (Lunt *et al*. 2017); the closest to this was an informal model-data comparison, considering

108   four climate models, known as the Eocene Model Intercomparison Project (EoMIP), undertaken by

109   Lunt *et al*. (2012). This work focused on temperature-based metrics, however another study by

110   Carmichael *et al*. (2016) used the same EoMIP ensemble to look at the hydrological cycle and

111   hydroclimate changes in response to the elevated CO_2 levels in the Eocene. The results focusing

112   specifically on Africa are discussed in more detail below but, globally, when compared to proxy data

113   it was found that the models generally underestimated precipitation over high latitudes, and those

114   models showing the most warming in these regions gave the best match to the data (Carmichael *et al*.

115   2016). Concerning the impact of elevated CO_2, it was found that all Eocene simulations showed a

116   more intense hydrological cycle (relative to the pre-industrial era, hereafter PI), with enhanced global

117   precipitation and evaporation, and that this was generally directly related to the elevated temperatures

118   resulting from higher CO_2 (Carmichael *et al*. 2016). At any given level of CO_2, global precipitation

119   changes varied widely between models, and certain regions (such as tropical Africa, discussed further

120   below) were found to be sensitive to which model was assessed (Carmichael *et al*. 2016).

121

122   However, a disadvantage (albeit unavoidable) to EoMIP was that there was no consistent framework

123   to the models' experimental design; each used different boundary conditions (e.g. palaeogeography)

124   and different levels of CO_2 (Lunt *et al*. 2012). To resolve this problem, therefore, more recently the

125   Deep Time Model Intercomparison Project (DeepMIP) was envisaged and conducted, using CMIP3

126   and CMIP5 models as well as some of the most recent state-of-the-art CMIP6-class models (Lunt *et*

127   *al*. 2017). The large-scale features coming out of the simulations are discussed in Lunt *et al*. (2021),

128   with several conclusions being drawn. Firstly, boundary conditions other than CO_2, discussed in

129   Section 2.1, contributed between 3-5°C of the global mean Eocene warming, relative to the PI (Lunt

130   *et al*. 2021). Secondly, the DeepMIP simulations showed less of a temperature spread than the

131   models in EoMIP, and an increase in climate sensitivity (Lunt *et al*. 2021). Lastly, when compared to

132   proxy SST data, most models reproduced the large-scale spatial patterns of the reconstructions but

133   still struggled at the regional scale, such as in the south-west Pacific (Lunt *et al*. 2021).

134

135   Similar to Lunt *et al*. (2012), Lunt *et al*. (2021) only focused on temperature and CO_2-based metrics.

136   The majority of recent studies looking at Eocene hydroclimate have focused on reconstructing

137   evidence for the Asian monsoon (e.g. Farnsworth *et al*. 2019, Ma *et al*. 2019, Quan *et al*. 2012, Xie *et*

al. 2019). There are very few studies, and in particular modelling studies, focusing on Africa. The aforementioned study by Carmichael *et al*. (2016) using the EoMIP ensemble found that tropical Africa was particularly sensitive to the model in question, and that the models varied in skill (when reproducing precipitation, relative to observations) in regions of relatively low precipitation such as over northern Africa's Sahel region. Moreover, although some models showed similar PI precipitation over tropical Africa, under Eocene conditions they were quite different (Carmichael *et al*. 2016). It should be noted, however, that this study did not actually include any early Eocene mean annual precipitation (MAP) reconstructions from Africa, only some Lutetian samples. More recently, Carmichael *et al*. (2018) ran several CO_2 simulations using just the UK Met Office Hadley Centre model HadCM3L, finding an increase in both the size and frequency of extreme precipitation events over equatorial and East Africa. Although MAP changes were relatively small, extreme rainfall increased by up to 70% over parts of tropical Africa, with summer precipitation events dominating the regime over southern Africa (Carmichael *et al*. 2018). Another example of Eocene African work is that of Liu *et al*. (2019), who looked at the Asian, African and Australian monsoons across five different time periods and found that the African monsoon existed as early as the mid-Paleocene. Keery *et al*. (2018) found the variability of the Asian and African monsoons during the Eocene was predominantly accounted for by orbital configuration changes such as the precession and obliquity; in DeepMIP, however, these were kept at PI values and so, here, the impact on the African monsoon will only be down to the CO_2 or the other boundary condition changes.

In this paper four main questions are addressed:

1) How well do the DeepMIP models' PI simulations reproduce modern observations of the African monsoon?
2) What is the impact of CO_2 and other Eocene boundary conditions on the African monsoon in the DeepMIP models' Eocene simulations?
3) What are the physical mechanisms behind this precipitation response?
4) How do the DeepMIP models' Eocene simulations compare with proxy data of the African monsoon?

Section 2 of this paper briefly describes the experimental design followed by the DeepMIP models, gives a brief introduction to the models themselves, and describes the observational and proxy data used for comparative purposes. Section 3 presents the results, addressing each of the above questions. Section 4 summarises and concludes.

2. EXPERIMENT DESIGN, MODELS, AND PROXY DATA
2.1. Experiment design

174   The full experimental design, which all DeepMIP modelling groups were required to follow as closely

175   as possible, is detailed extensively in Lunt *et al*. (2017) and so will only be briefly outlined here. In

176   addition to the various CO_2 experiments, all modelling groups were required to carry out a PI

177   simulation for comparison purposes, which was to be as close as possible to the CMIP6 standard

178   *piControl* simulation (Eyring *et al*. 2016).

179

180   For the Eocene simulations, a number of boundary conditions needed to be changed, the key ones for

181   the African region of which are shown in fig_ancils.

182

183
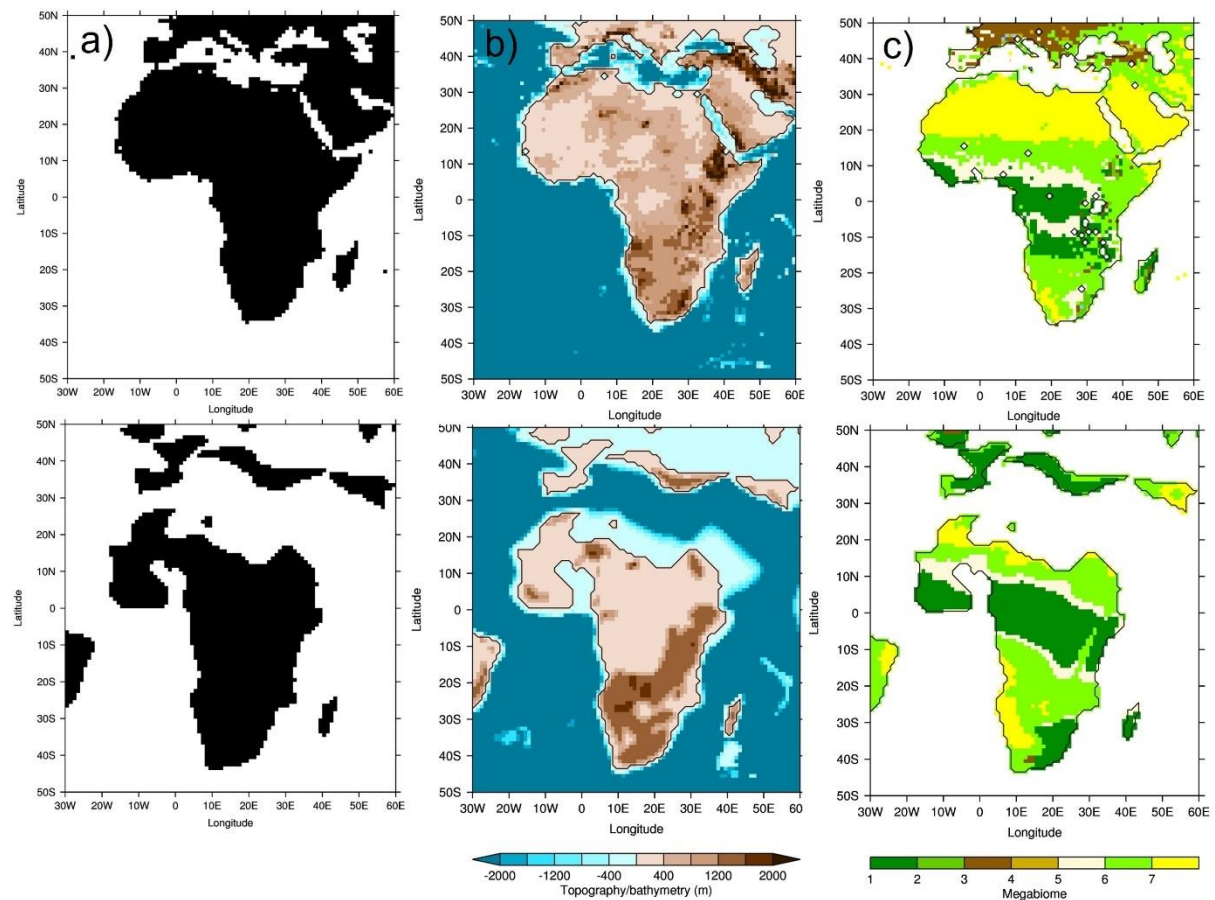
184   Figure 1 – Main boundary conditions changed in DeepMIP simulations, where top row = PI and bottom row =

185   Eocene: a) Land sea mask; b) Topography/bathymetry; c) Vegetation, expressed as megabiomes according to

186   Harrison and Prentice 2003 (where 1 = Tropical, 2 = Warm-temperate, 3 = Temperate, 4 = Boreal, 5 = Savanna,

187   6 = Grassland and 7 = Desert). The PI topography/bathymetry is taken from ETOPO5, re-gridded to 1°x1°

188   resolution, whereas the other fields are from Herold *et al*. (2014)

189

190   Firstly, the land sea mask (LSM) was based on the palaeogeographic heights (discussed further

191   below), with possible manual manipulation required in some models to maintain the various gateways

192   (Lunt *et al*. 2017). The new LSM produced a geographically smaller Africa relative to the PI, with

193   much of the present-day landmass north of 20°N being ocean in the Eocene due to the increased sea

6

194 level (Figure 1a). Secondly, the palaeogeography (including topography and bathymetry) was based

195 on the digital reconstruction of the early Eocene from Herold *et al*. (2014), with the topography (and

196 sub-grid scale topography) being applied as an absolute value rather than as an anomaly (Lunt *et al*.

197 2017). Over Africa, the most pronounced changes were over southern and eastern Africa, with

198 generally larger areas of raised topography in the Eocene, relative to the PI (Figure 1b). This can be

199 seen more clearly in the Supplementary Material, where the differences in topography are shown;

200 there is clearly a large increase in elevation over western Africa where there is land in the Eocene but

201 ocean in the PI, but apart from this (where the landmasses coincide) the largest changes are over

202 southern and eastern Africa (Figure S1). Thirdly, concerning the land surface, vegetation and river

203 run-off routing was also based on the dataset of Herold *et al*. (2014), using an appropriate lookup

204 table to convert the vegetation megabiomes into whatever format was required by the model (Lunt *et*

205 *al*. 2017). The Eocene vegetation was created by running the dynamic vegetation model BIOME4

206 (Kaplan *et al*. 2003), itself forced by Eocene atmospheric conditions from another climate model run

207 and, as Herold *et al*. (2014) note, although the simulated vegetation compares well with

208 reconstructions, over certain regions such as South Africa a lack of records meant validation was not

209 possible. When compared to the PI, over Africa the new vegetation resulted in: i) a loss of the desert

210 regions over the present-day Sahara, primarily because this is ocean in the Eocene; ii) a latitudinal

211 expansion (relative to the PI) of tropical rainforest across central Africa; and iii) an addition of a large

212 area of tropical rainforest over southern Africa, which is savanna or grassland in the PI (Figure 1c).

213 However, some features remained similar in the Eocene relative to the PI, such as the region of

214 tropical rainforest across central Africa being bordered by savannah to the north and south, and the

215 Namib Desert (Figure 1c). The impact on precipitation of these three boundary condition changes is

216 discussed below. Soil parameters, including soil dust fields, were given a globally constant value, and

217 (given the lack of palaeodata) no lakes were prescribed unless dynamically predicted (Lunt *et al*.

218 2017). Concerning greenhouse gas concentrations, the CO_2 experiments were divided into a set of

219 standard experiments (which all modelling groups should ideally have conducted) and a set of

220 sensitivity experiments (which were optional). All of these were expressed as multiples of the PI

221 simulation, typically with a CO_2 of 280 ppmv, and were as follows: 3x and 6x the PI for the standard

222 experiments, and 1x, 1.5x, 2x, 4x and 9x the PI for the sensitivity experiments (Lunt *et al*. 2017). See

223 Table 1 for which modelling groups conducted which experiments. All other greenhouse gases were

224 kept as PI, the justification for which is given in Lunt *et al*. (2017). Concerning aerosols, given the

225 rapid development of representation of aerosols in models the experimental design was flexible here

226 and allowed modelling groups to either leave these as PI, treat aerosols interactively (if possible),

227 prescribe aerosols from Herold *et al*. (2014), or a combination of the above (Lunt *et al*. 2017). The

228 solar constant and astronomical parameters were kept identical to the PI, the justification for which is

229 again given in Lunt *et al*. (2017).

230

Modelling group responsible	Model	Atmospheric resolution (lon x lat)	CO₂ experiments undertaken	Run length (years)	References
University of Michigan, US	CESM1.2_CAM5	2.5° x 1.89°	1x, 3x, 6x, 9x	2000	Hurrell *et al.* 2013
Polish Academy of Sciences, Poland	COSMOS-landveg_r2413	3.75° x 3.71°	1x, 3x, 4x	9500	Roeckner *et al.* 2003
Stockholm University, Sweden	GFDL_CM2.1	3.75° x 3.05°	1x, 2x, 3x, 4x, 6x	6000	Delworth *et al.* 2006
University of Bristol, UK	HadCM3B_M2.1aN	3.75° x 2.5°	1x, 2x, 3x	7800	Valdes *et al.* (2017)
University of Bristol, UK	HadCM3BL_M2.1aN	3.75° x 2.5°	1x, 2x, 3x	7800	Valdes *et al.* (2017)
National Academy of Sciences, Russia	INM-CM4-8	2° x 1.5°	6x	1050	Volodin *et al.* (2018)
Laboratoire des Sciences du Climat et de l'Environnement, France	IPSLCM5A2	3.75° x 1.89°	1.5x, 3x	4000	Sepulchre *et al.* (2020)
University of Tokyo, Japan	MIROC4m	2.8125° x 2.79°	1x, 2x, 3x	5000	Chan *et al.* (2011)
University of Bergen, Norway	NorESM1_F	2.5° x 1.89°	2x, 4x	2100	Guo *et al.* (2019)

231

232   Table 1 - Models taking part in DeepMIP, including relevant details and references

233

234   Lastly, the experimental design provided some advice on practical matters such as simulation length

235   and output format. The simulations varied in length (see Table 1) but were all at least 1000 years in

236   length, with the climatologies, comprising the results discussed here, being calculated over the final

237   100 years. At that point, all simulations should have had a global mean top-of-the-atmosphere (TOA)

238   net radiation balance of less than 0.3 W m^{-2} (or a similar balance to that of the PI) and an SST trend of

239   less than 0.1°C century^{-1} (Lunt *et al.* 2017). All of the output, details of which are given in Lunt *et al.*

240   (2017), were uploaded to a centralised DeepMIP database.

241

242   **2.2. Models**

243   Extensive details on each model, and how the experimental design was implemented in their

244   simulations, are given in Lunt *et al.* (2021) and references therein and will therefore only briefly be

245   discussed here; those aspects likely to affect monsoon precipitation (e.g. convection and land-surface

246   schemes) will be focused upon here. In total, nine models were included in DeepMIP, although it

247   should be noted that two of these are different configurations of the same model. See Table 1 for a

248   list of the models, along with their atmospheric spatial resolutions and appropriate references

249 (particularly relating to the atmospheric component of the models and elements relating to

250 hydroclimate, where available). In detail, these are as follows.

251

252 • CESM1.2_CAM5: The Community Earth System Model version 1.2 (CESM1.2) is comprised

253 of the Community Atmosphere Model version 5.3 (CAM5), the Community Land Model

254 version 4.0, the Community Ice Code version 4.0 and the Parallel Ocean Program version 2

255 (Hurrell *et al*. 2013). CAM5 uses the finite-volume dynamical core and physical

256 parameterizations of deep convection (Zhang and McFarlane 1995), shallow convection and

257 moist turbulence (Park and Bretherton 2009), and cloud microphysics (Morrison and

258 Gettelman 2008). This version contains new physical parameterisations in the atmosphere,

259 such as the cloud microphysics, which is critical for the simulation of the large-scale climate

260 features of the early Eocene (Liu *et al*. 2017)

261 • COSMOS-landveg_r2413: For an atmospheric general circulation model, ECHAM5 (the

262 European Centre Hamburg Model) is used (Roeckner *et al*. 2003), and this is coupled to the

263 Max-Planck-Institute for Meteorology Ocean Model (MPIOM) (Marsland *et al*. 2003); the

264 coupled model is described by Jungclaus *et al*. (2006). COSMOS-landveg_r2413 simulates

265 cumulus convection using a mass flux scheme. The orography is represented in spectral

266 domain by surface geopotential (see Stepanek and Lohmann 2012 for more details regarding

267 model description). The land surface conditions for each biome are based on Hagemann

268 (2002); additionally, parameters with a seasonal cycle (i.e. leaf area index and vegetation

269 ratio) in the latitude belt of ~20°S-20°N were smoothed and an annual average for each biome

270 was prescribed.

271 • GFDL_CM2.1: This uses the Geophysical Fluid Dynamics Laboratory (GFDL) CM2.1 model

272 (Delworth *et al*. 2006), with modifications as described in Hutchinson *et al*. (2018), and

273 comprising the Atmosphere Model 2, Land Model 2 and the Sea Ice Simulator 1, coupled to

274 the ocean component from the modular ocean model version 5.1 (MOM5.1). The atmosphere

275 uses a finite-volume discretisation, and a 3° latitude x 3.75° longitude resolution with 24

276 vertical levels, following the configuration of CM2Mc (Galbraith *et al*. 2011). Convection is

277 parameterised by the relaxed Arakawa-Schubert scheme of Moorthi and Suarez (1992), with a

278 lower-bound on entrainment as specified in Tokioka *et al*. (1988). Cloud microphysics are

279 parameterised using the scheme of Rotstayn (1997), while cloud macrophysics use the

280 parameterisation of Tiedtke (1993). Full details of the convection and cloud

281 parameterisations are given in Delworth *et al*. (2006). Of possible relevance to the simulation

282 of precipitation, the topography is smoothed using a three-point mean filter to allow a

283 smoother interaction with the wind field (Lunt *et al*. 2021).

- HadCM3B_M2.1aN: This Hadley Centre Climate Model (HadCM3) version is documented extensively in Valdes *et al*. (2017). In particular, the model uses a single 'bulk' cloud model to parameterise dry as well as shallow and deep moist convection (Grant 1998). The cloud scheme uses a statistical parametrization via a probability density function over the grid-box total water content (Bushell 1998). Six short-wave and eight long-wave radiation bands are represented by the scheme of Edwards and Slingo (1996). Static fields for the nine surface types of the MOSES2.1 land surface scheme (Cox *et al*. 1999) are derived from the ten megabiomes of the DeepMIP vegetation boundary conditions (Herold *et al*. 2014) via a lookup table. The atmosphere uses a Cartesian grid with a horizontal resolution of 3.75 x 2.5° (longitude x latitude) and 19 hybrid vertical levels.

- HadCM3BL_M2.1aN: The only difference between this version of HadCM3 and the one described above is the horizontal resolution of the ocean component (Cox 1984), at 1.25° x 1.25° for HadCM3B_M2.1aN and 3.75° x 2.5° for HadCM3BL_M2.1aN, and associated diffusion parameters (Valdes *et al*. 2017). Both versions use 20 unequally spaced vertical levels in the ocean ranging between 10 and 616 m.

- INM-CM4-8: This version of the Institute of Numerical Mathematics (INM) model is described in Volodin *et al*. (2018), but the parameterisations of physical processes are the same as in the previous version, INM-CM5, and described more detail in Volodin *et al*. (2017). Parameterization of condensation and cloud formation follows Tiedtke (1993), and cloud water is a prognostic variable. Parameterization of cloud fraction follows Smagorinsky (1963); cloud fraction is a diagnostic variable, independent of the calculation of condensation, and depended on the relative humidity. Deep and shallow convection is parameterized by Bets (1986). The surface, soil and vegetation scheme follow Volodin and Lykossov (1998), with the evolution of the equations for temperature, soil water and soil ice being solved at 23 levels from the surface to 10 meters depth (Volodin *et al*. 2018). The fractional area of 13 types of potential vegetation is specified, and actual vegetation as well as LAI is calculated according to the soil water content in the root zone and soil temperature (Volodin *et al*. 2018).

- IPSLCM5A2: The IPSL-CM5A2 Earth system model from the Institut Pierre Simon Laplace (IPSL) is documented by Sepulchre *et al*. (2020), and is based on the previous generation IPSL Earth system model (IPSLCM5A, Dufresne *et al*. 2013) but with new revisions such as a re-tuning of global temperature. It comprises the LMDZ5 (Laboratoire de Météorologie Dynamique Zoom) atmosphere model, the Organising Carbon and Hydrology In Dynamic Ecosystems (ORCHIDEE) land surface and vegetation model and the Nucleus for European Modeling of the Ocean (NEMOv3.6) ocean model, which includes the LIM2 sea ice model and the Pelagic Interactions Scheme for Carbon and Ecosystem Studies (PISCESv2) biogeochemical model (Lunt *et al*. 2021). LMDZ5 runs at a horizontal resolution of 1.9° ×

320   2.5° (latitude × longitude) with 39 hybrid sigma-pressure levels. The LMDZ5 radiation

321   scheme is inherited from the European Center for Medium-Range Weather Forecasts

322   (Fouquart and Bonnel 1980, Morcrette et al. 1986), and the dynamical effects of the subgrid-

323   scale orography are parameterized according to Lott (1999). Turbulent transport in the

324   planetary boundary layer is treated as a vertical eddy diffusion (Laval et al. 1981), with

325   counter-gradient correction and dry convective adjustment, and the surface boundary layer is

326   treated according to Louis (1979). Cloud cover and cloud water content are computed using a

327   statistical scheme (Bony and Emanuel 2001). For deep convection, the LMDZ5A version

328   uses the "episodic mixing and buoyancy sorting" scheme originally developed by Emanuel

329   (1991).

330 •   MIROC4m: This version of the Model for Interdisciplinary Research on Climate (MIROC) is

331   documented by K-1 model developers (2004) and summarized in Chan *et al*. (2011). In the

332   atmosphere model, cumulus parameterization is based on Arakawa and Schubert (1974), with

333   some simplifications and the cloud base mass flux is treated as a prognostic variable.

334   Cumulus convection is suppressed when the cloud-mean ambient relative humidity is less

335   than the critical value of 0.8. The land surface model (Minimal Advanced Treatments of

336   Surface Interaction and Runoff, MATSIRO) is documented by Takata *et al*. (2003), where

337   prognostic variables include canopy temperature, canopy water content, snow amount, soil

338   moisture content and frozen soil moisture content. Fixed vegetation types are specified over

339   ice-sheet-free. The ocean component is version 3.4 of the CCSR (Center for Climate System

340   Research) Ocean Component Model (COCO), documented in Hasumi (2000).

341 •   NorESM1_F: This version of the Norwegian Earth System Model (NorESM) is described in

342   detail in Guo *et al*. (2019) and Li *et al*. (2020), and differs from the previous version

343   (NorESM1-M) in that while it has the same atmosphere-land grid, the ocean and sea ice

344   components use a tripolar grid (rather than the bipolar grid in NorESM1-M), resulting in a

345   more realistic Atlantic Meridional Overturning Circulation (Lunt *et al*. 2021). NorESM1_F

346   couples the Miami Isopycnic Coordinate Ocean Model (MICOM) and the spectral

347   Community Atmosphere Model (CAM4) (Eaton 2010, Neale *et al*. 2008, Neale *et al*. 2013).

348   CAM4 includes the Zhang and McFarlane (1995) deep convection scheme, the Hack (1994)

349   shallow convection scheme, the nonlocal boundary layer scheme of Holtslag and Boville

350   (1993) and the representation of cloud microphysics and macrophysics by Rasch and

351   Kristjánsson (1998) and Zhang *et al*. (2003). Instead of using the undiluted convective

352   available potential energy (CAPE) in the original deep convection scheme, the diluted CAPE

353   through an explicit representation of entrainment has been used to close the cumulus

354   parameterization (Neale *et al*. 2008). The convective momentum transport has also been

355   included in the parameterization of deep convection (Richter and Rasch 2008). Additionally,

356   NorESM1_F adopts energy updates and energy conservation. Compared to NorESM1-M,

357   NorESM1_F has several important improvements on how precipitation is simulated, such as

358   improvements in seasonality, a reduced wet bias and mitigation of the common double

359   intertropical convergence zone (ITCZ) problem (Li *et al.* 2020).

360

361 **2.3. Observational and proxy data**

362 Here the observational and proxy data are described; firstly there is a description of the modern,

363 satellite-derived data used to assess and evaluate the PI simulations, and secondly there is a

364 description of the Eocene proxy data used to evaluate the Eocene simulations.

365

366 *2.3.1. Satellite-derived rainfall estimates from the modern period*

367 Even in the 21st century, there is a severe lack of in-situ rain gauge data over Africa; South Africa is

368 probably the best populated in terms of rainfall measurements, but in other countries such as Angola

369 or Namibia rain gauge data are sparse or non-existent (e.g. Williams *et al.* 2007, Williams *et al.* 2008,

370 Williams *et al.* 2010). The CenTrends precipitation dataset (Funk *et al.* 2015) contains measurements

371 going back to 1900, but only for a small number of countries in East Africa. Likewise, although the

372 Global Historical Climate Network (GHCN) database (Durre *et al.* 2008, Durre *et al.* 2010, Menne *et*

373 *al.* 2012) does contain temperature measurements going back to 1861, precipitation measurements do

374 not begin until the 1950s and are again relatively sparse in Africa. Therefore, a possible solution to

375 the problem of data unavailability is to use satellite-derived rainfall estimates (SREs), which offer

376 near-uniform coverage at relatively high spatial resolution from the 1980s onwards.

377

378 Several datasets of SREs currently exist, but here the Tropical Applications of Meteorology using

379 SATellite data and ground-based observations (TAMSAT) is used. TAMSAT (version 3.1) provides

380 daily, 10-daily, monthly and seasonal precipitation estimates over Africa at 4 km resolution, and

381 extends from 1983 to the present-day. The data are publicly available; please see Data Availability

382 and Maidment *et al.* (2014), Maidment *et al.* (2017) and Tarnavsky *et al.* (2014) for details. Here,

383 TAMSAT is used as a comparative tool for evaluating the PI simulations of the DeepMIP models. A

384 caveat here is that the models are showing precipitation simulated under PI boundary conditions,

385 whereas TAMSAT is showing precipitation from the late 20th and early 21st century (referred to here

386 as modern) and will therefore contain an anthropogenic signal; this, however, is unavoidable given the

387 lack of PI precipitation observations. It is expected that the biases between comparing the models to

388 PI precipitation versus comparing them to modern precipitation will be less than the biases between

389 the models themselves (i.e. the inter-model spread), and indeed much less than the uncertainty

390 associated with the Eocene reconstructions.

391

392 *2.3.2. Palaeobotanical Eocene precipitation estimates*

393   The distribution and physiognomy of land plants are sensitive to precipitation (Wright *et al.* 2017).

394   Therefore, the taxonomic affinity and the morphology of leaf fossils can be used to generate palaeo-

395   precipitation estimates (e.g. Utescher *et al.* 2014, Wilf *et al.* 1998). For this study, previously

396   established Paleocene-Eocene palaeobotanical records from Africa were compiled (see

397   Supplementary Material, Table S1). The distribution of the nearest living relatives (NLR) of these

398   taxa was then analyzed using the bioclimatic analysis approach to find the highest probability

399   precipitation range in which all taxa could co-occur (e.g. West *et al.* 2020, Willard *et al.* 2019).

400

401   Geodetic coordinates of occurrences were obtained for the NLR of each plant group from the Global

402   Biodiversity Information Facility (GBIF) (see Supplementary Material, Table S2). These occurrence

403   datasets were then filtered for uncertain, exotic and superfluous occurrences, as well as subjected to a

404   random resampling to avoid regional overrepresentation of densely sampled areas. A climatic

405   envelope for each plant group (see Table S2) was then generated by extracting precipitation data

406   (mean annual precipitation (MAP), wettest month (WMP), driest month (DMP), warmest and coldest

407   quarter precipitation (WQP and CQP, respectively) and the precipitation seasonality coefficient (PS))

408   using the DISMO package in R (Hijmans *et al.* 2005). A probability density function was then

409   generated for each co-occurring plant group by testing the likelihood of the plant group occurring at

410   100,000 unique extant combination of MAP, WMP, DMP, PS, WQP and CQP. As shown in

411   Equation 1, the product of probabilities (f) was calculated for each plant group (t) at each climatic

412   combination (x), using the means (μ) and standard deviations (σ) of their modern-day bioclimatic

413   envelope, for each climatic variable (c).

414

415
$$f(t_n) = \prod_{i=1}^{6} \frac{1}{\sqrt{2\sigma_c^2 \times \pi}} e^{x_c - \mu_c / 2\sigma_c^2}$$

416   Equation 1

417

418   A combined likelihood for all plant groups in the assemblage combined can then be calculated with

419   the product of all likelihoods (n), shown in Equation 2.

420

421
$$f(z) = \prod_{i=1}^{n} t_n$$

422   Equation 2

423

424   The combination of MAP, WMP, DMP, PS, WQP and CQP with the highest likelihood is the value

425   reported here as most representative for the assemblage, and the highest and lowest values of the

13

426 metrics with f(z) ≥ 5% of the maximum f(z) is represented as the uncertainty (using the 95%

427 confidence interval).

428

429 Eleven plant assemblages from South Africa, Tanzania, South Sudan, Cameroon, Côte d'Ivoire,

430 Ghana and Nigeria were analyzed with the bioclimatic analysis NLR method (Adeonipekun *et al*.

431 2012, Atta-Peters and Salami 2004, Cantrill *et al*. 2013, Chiaghanam *et al*. 2017, de Villiers 1997,

432 Eisawi and Schrank 2008, Goha *et al*. 2016, Okeke and Umeji 2016, Salami 1984, Salard-Cheboldaeff

433 1979, Uzodimma 2013).

434

435 The NLR generated precipitation values were supplemented with an additional value based on leaf

436 area analysis (LAA) derived data by Jacobs and Herendeen (2004) and Kaiser *et al*. (2006), also from

437 Tanzania. In locations where the final results are in the same geographical location, the

438 reconstructions were averaged. The final results of this analysis are shown in Table 2, with Eocene

439 MAP expressed as ranges and modern MAP taken from TAMSAT.

440

Site name	Latitude (°N)	Longitude (°E)	MAP (mm year⁻¹)	
			Eocene range	**Modern**
Koningsnaas, South Africa	-30.2	17.3	1318-1738	101
Shagamu, Nigeria	6.7	3.7	1148-2089	1762
Melut Basin, South Sudan	10	33	1175-1905	757
Kwakwa, Cameroon	4.5	9.1	1175-1905	2524
Mwadui, Tanzania	-3.9	33.5	813-1738	754
Tano, Ghana	4.7	-3	1514-2344	-
Nanka, Nigeria	6.12	7	1380-2291	1683
Abidjan margin, Côte d'Ivoire	5	-4.1	1660-1950	-
Okigwe, Nigeria	5.82	7.34	1175-1862	2311
Bende - Umuahia, Nigeria	5.47	7.45	1514-2291	2311
Araromi, Nigeria	7.7	3.5	1072-1738	1179
Mahenge, Tanzania	-4.79	34.26	720-800	707
Mahenge, Tanzania	-4.79	34.26	630-690	707
Mahenge, Tanzania	-4.79	34.26	737-815	707

Mahenge, Tanzania	-4.79	34.26	644-708	707
Mahenge, Tanzania	-4.79	34.26	710-790	707
Mahenge, Tanzania	-4.79	34.26	610-680	707
Mahenge, Tanzania	-4.79	34.26	610-680	707
Mahenge, Tanzania	-4.79	34.26	740-820	707

441

442 Table 2 - Locations and mean annual precipitation (MAP) from Eocene palaeobotanical records from Africa,

443 and modern values. Eocene ranges of MAP are expressed as the 95% confidence interval for all locations

444 except Mahenge, where ranges are expressed as +/- 1 standard deviation.   Modern values of MAP taken from

445 TAMSAT; missing values indicate ocean regions, as TAMSAT MAP is land only

446

447 **3. RESULTS**

448 Here the results of different comparisons are described: i) a model validation exercise, where the

449 models' PI simulations are compared to modern observations (Section 3.1); ii) a simulation

450 comparison, where precipitation from the models' Eocene simulations, at varying levels of CO_2, is

451 compared (Section 3.2); iii) a simulation comparison, where the physical mechanisms behind the

452 precipitation response are investigated (Section 3.3); and iv) a model-data comparison, where

453 precipitation from the models' Eocene simulations is compared to available proxy data (Section 3.4).

454

455 **3.1. DeepMIP models' preindustrial simulations versus modern observations**

456 Here the focus is on mean precipitation differences between the various DeepMIP PI simulations

457 (including the multi-model ensemble mean, MME) and precipitation observations from TAMSAT

458 (see Section 2.3.1). Precipitation anomalies (PI simulations - TAMSAT) during the core West

459 African monsoon period (June-August, JJA) are shown in Figure 2, where the models have been

460 ordered according to the root mean square error (RMSE), relative to TAMSAT. Two observations are

461 noteworthy. Firstly, the MME is showing by far the closest agreement to TAMSAT, with a much

462 lower RMSE (by ~10 mm month^{-1} less than even the next lowest individual model), highlighting the

463 importance of using the MME to counterbalance individual models' biases (whether they be under or

464 overestimating). The MME will therefore subsequently be used when discussing the various Eocene

465 simulations. Secondly, there appears to be a divide between: a) models such as IPSLCM5A2, INM-

466 CM4-8 and COSMOS-landveg_r2413 that are underestimating African precipitation (i.e. are showing

467 drier conditions across West Africa at ~10°N), which have relatively low RMS error compared with

468 TAMSAT; and b) models such as HadCM3BL_M2.1aN, MIROC4m and GFDL_CM2.1 that are

469 overestimating African precipitation, which have relatively high RMS error compared with

15

470 TAMSAT. For example, the model with the least agreement (GFDL_CM2.1, RMSE = 70.6 mm

471 month^{-1}) is overestimating precipitation over West Africa by more than 100 mm month^{-1}.

472

	RMSE
MME	23.90
NorESM1_F	32.96
IPSLCM5A2	42.14
INM-CM4-8	42.21
COSMOS-landveg_r2413	43.26
COSMOS-landveg_r2413 (TO)	43.37
HadCM3B_M2.1aN	43.41
CESM1.2_CAM5	43.84
HadCM3BL_M2.1aN	53.91
MIROC4m	56.69
GFDL_CM2.1	70.64

473
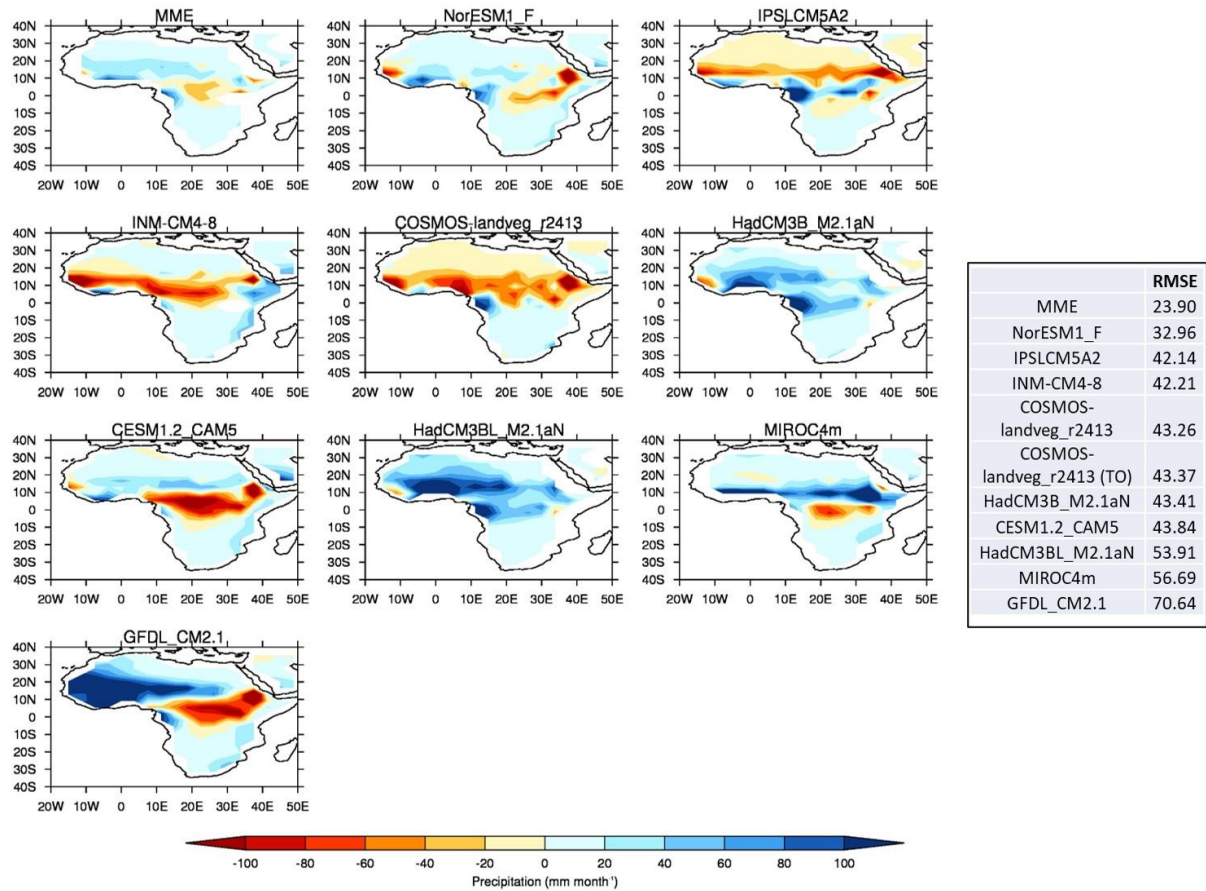
474 Figure 2 - JJA precipitation climatology differences (PI simulations - TAMSAT), re-gridded to lowest common

475 spatial resolution (that of COSMOS-landveg_r2413) and ordered according to Root Mean Squared Error

476 (RMSE, in mm month^{-1}, see insert). RMSE calculated over 20°W-50°E, 40°N-40°S, land points only

477

478 Concerning the seasonal and latitudinal distribution of African precipitation, Figure 3 shows the

479 annual cycle of West African (defined here as land points only encompassing 20°W-15°E, 0-20°N)

480 precipitation and the zonal mean of JJA West African precipitation (Figure 3a and b, respectively).

481 Outside of the JJA monsoon season, the majority of models are overestimating precipitation

482 throughout the year (Figure 3a), with the model closest to TAMSAT (in terms of the seasonal cycle

483 i.e. precipitation timings) being CESM1.2_CAM5, although even this model overestimates

484 precipitation during the first half of the year. When averaged over this region, only one model (INM-

485 CM4-8) underestimates precipitation throughout the year, but is nevertheless closer to TAMSAT than

486 those which overestimate, in agreement with that discussed above and shown in Figure 2. One model

487 (GFDL_CM2.1) greatly overestimates precipitation especially during the monsoon season, and others

488 (such as INM-CM4-8) underestimate precipitation during the monsoon season and therefore do not

489 correctly reproduce the strong seasonality (i.e. the precipitation curve is flatter); for example, the

16

490   difference between the wettest and driest month in this model is 136 mm month^{-1}, whereas it is 161

491   mm month^{-1} in TAMSAT and 181 mm month^{-1} in the MME (Figure 3a). The MME also

492   overestimates precipitation throughout the year but is nevertheless closer to TAMSAT in terms of

493   seasonality than many of the wetter models (Figure 3a). Latitudinally, most models are showing a

494   much wider (in terms of latitudinal extent) rain belt relative to TAMSAT, with GFDL_CM2.1 and the

495   HadCM3 family in particular not reproducing the observed rapid drop-off in precipitation either near

496   the Equator or north of 15°N (Figure 3b). In part due to some drier models approaching the Equator

497   (such as CESM1.2_CAM5 and INM-CM4-8), the MME is showing a similar latitudinal extent of

498   precipitation compared to TAMSAT, and while it is still too wet at low latitudes it does correctly drop

499   off north of 15°N (Figure 3b).

500
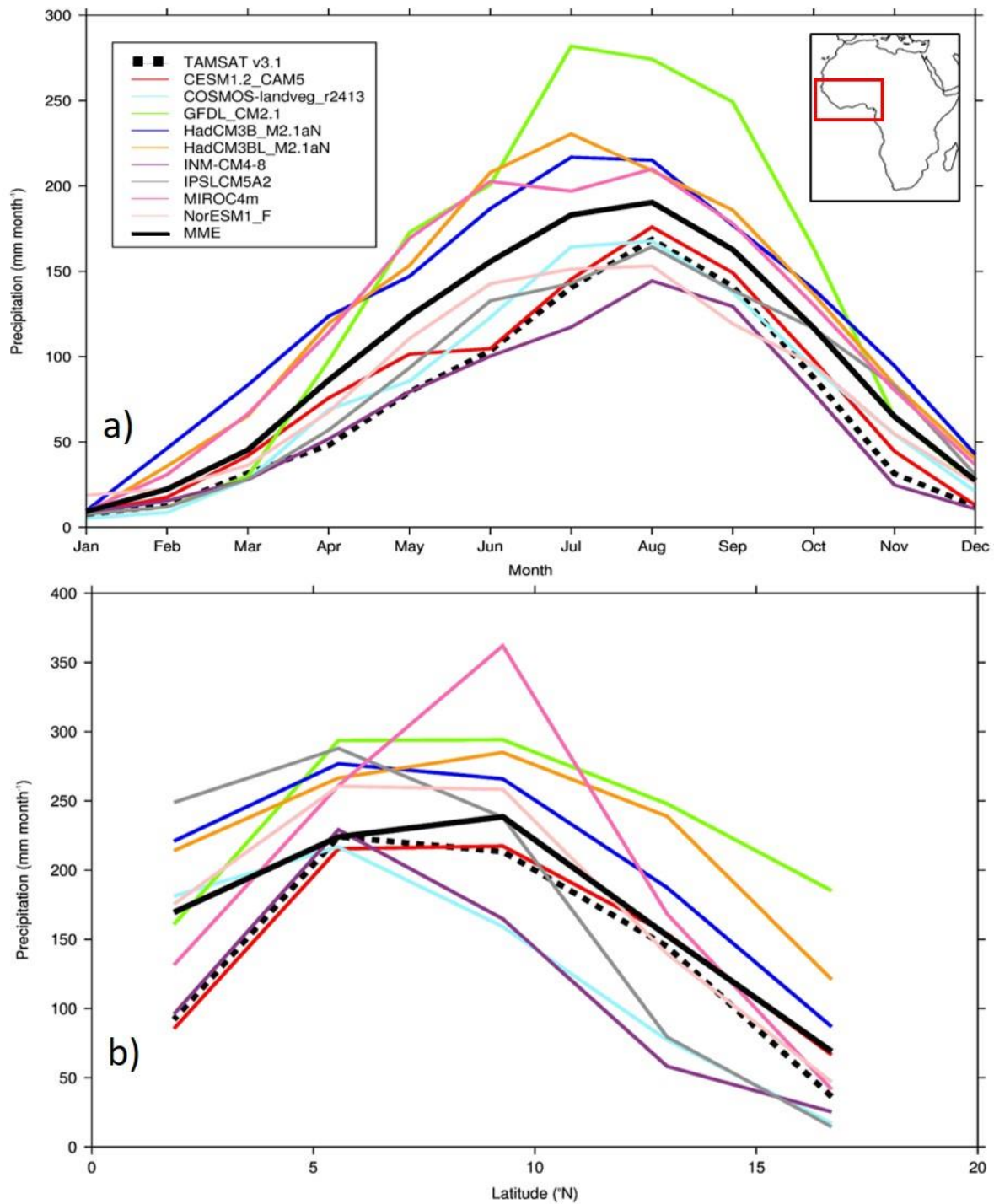
Figure 3 - Precipitation climatology from TAMSAT and PI simulations, averaged over West Africa (20°W-15°E, 0-20°N - land points only): a) Mean seasonal cycle, at each model's individual spatial resolution; b) Zonal mean of JJA precipitation, re-gridded to lowest common spatial resolution

3.2. DeepMIP models' Eocene simulations relative to preindustrial simulations and each other

Here the focus is on mean precipitation differences between various DeepMIP Eocene CO_2 sensitivity experiments, in which all boundary conditions other than CO_2 were kept identical. The focus is not

18

510   only on the precipitation response to varying CO_2 concentrations relative to the PI simulations, but

511   also from each CO_2 experiment individually (relative to each other). Precipitation anomalies of all the

512   CO_2 experiments versus PI are firstly briefly presented (Section 3.2.1), and then the experiment

513   results are divided into a non-CO_2 component (i.e. the impact of the other boundary condition

514   changes, Section 3.2.2) and a CO_2 component (Section 3.2.3).

515

516   *3.2.1. All CO_2 experiments versus preindustrial*

517   The precipitation anomalies (Eocene - PI), for each CO_2 experiment and for each model during JJA

518   are shown in Figure 4. This is only briefly presented, because the combination of a palaeogeographic

519   forcing and a CO_2 forcing makes interpretation difficult; this is why the results are broken down into a

520   non-CO_2 component and CO_2 component below. It should be noted that when the MME is discussed

521   below (see Sections 3.2.2 and 3.2.3), only models that participated in the particular experiment are

522   included.

523

524
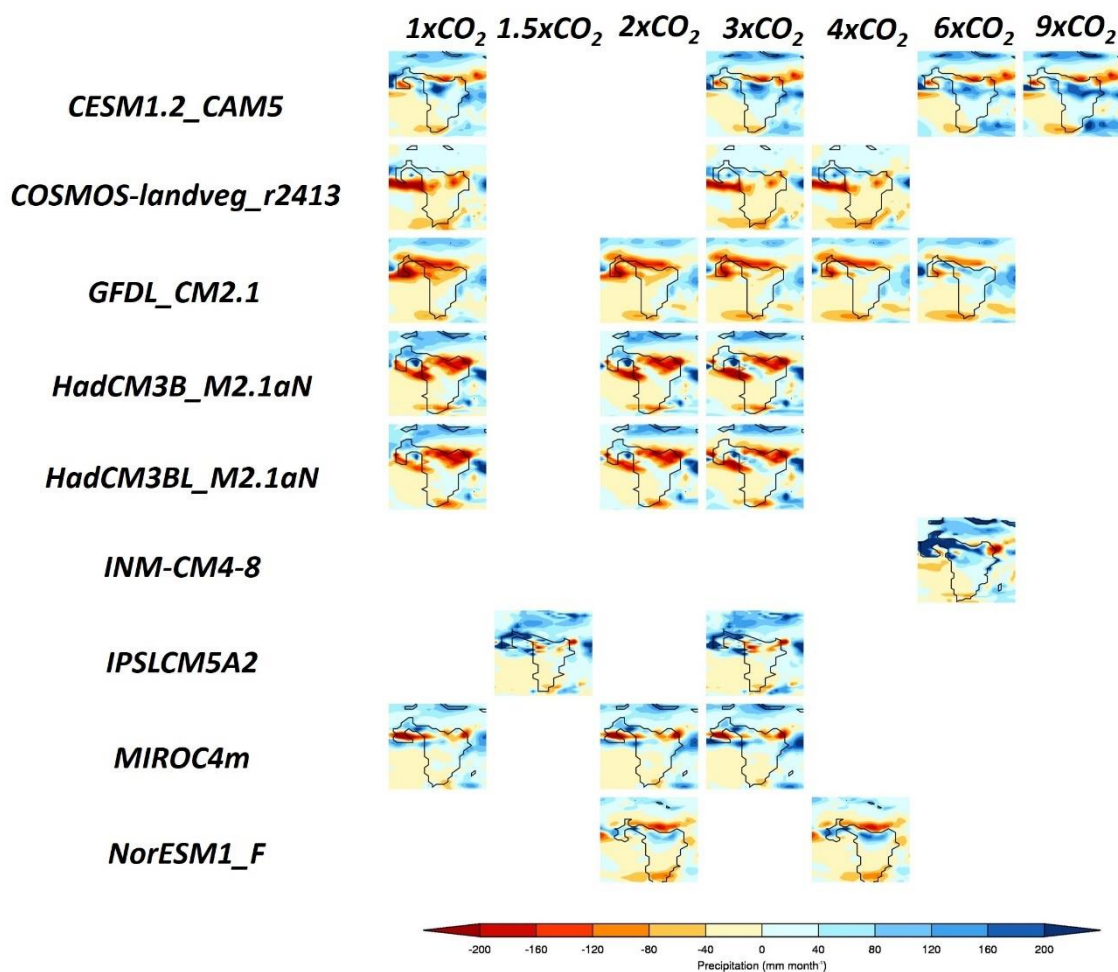
525   Figure 4 - JJA precipitation climatology differences (Eocene - PI), for each CO_2 simulation from each model

526

527   There is no clear linear trend in either wetting or drying across Eocene Africa as the CO_2

528   concentrations increase (Figure 4). Although many models show drying (relative to the PI) of up to

529   ~180 mm month^{-1} across northern and western Africa in the 1x, 2x and 3x experiments, this gradually

530   disappears as higher CO_2 concentrations are applied, with some models showing precipitation

531   increases of over 200 mm month^{-1} (Figure 4). Some models disagree regardless of experiment, such

532   as GFDL_CM2.1 which shows drying over northern Africa in all CO_2 experiments contrasting with

533   IPSLCM5A2 which shows wetting over northern Africa in all CO_2 experiments. Further south, none

534   of the models in any of the experiments are showing a large precipitation response. In very general

535   terms, however, at the lower levels of CO_2 concentrations (i.e. up to 4x) the majority of models are

536   showing the same region of drying over northern and western Africa.

537

538   *3.2.2. 1x CO_2 experiment versus preindustrial: impact of non-CO2 boundary conditions*

539   The 1x CO_2 experiment versus PI is of particular interest, because this shows the impact of the other

540   boundary conditions rather than that from CO_2 concentrations. When CO_2 concentrations are kept as

541   PI (as in the 1x experiment), the boundary conditions (see Section 2.1) likely to have the largest

542   impact on regional precipitation are the LSM, topography and vegetation (see Figure 1). Although

543   land ice changes, the largest of which during the Eocene were over the Antarctic Ice Sheet (AIS), do

544   cause a precipitation response (e.g. Kennedy-Asser *et al*. 2019), this is thought to be a mainly local

545   signal and further afield, such as over northern and western Africa during JJA, there is little or no

546   precipitation change when the AIS is either imposed or removed (Kennedy-Asser, pers. comm.).

547

548   The MME precipitation anomaly for this experiment is shown in Figure 5a; it should be noted that,

549   although six models conducted this experiment (CESM1.2_CAM5, COSMOS-landveg_r2413,

550   GFDL_CM2.1, HadCM3B_M2.1aN, HadCM3BL_M2.1aN and MIROC4m), only the latter four are

551   included here in the MME, to be consistent with the analysis of the CO_2 component (Section 3.2.3).

552   From the available DeepMIP results, it is impossible to disentangle the boundary conditions and

553   ascertain which is dominant in causing the precipitation response; in an ideal world, sensitivity

554   experiments would be conducted to introduce each boundary condition individually, but this is not

555   possible with the results currently available on the DeepMIP database. Nevertheless, based on the

556   results it is possible to theorise which of these boundary conditions might be causing this MME

557   precipitation response. The largest precipitation changes relative to the PI are a small increase in

558   precipitation to the north of Eocene Africa and in the western Indian Ocean, and a decrease in

559   precipitation over western and northern equatorial Eocene Africa (Figure 5a). It is likely that the

560   northern increases are caused by the change in the LSM (Figure 1a) as this region comprises the

561   preindustrial (and modern) Sahara but is ocean in the Eocene and therefore would have been a much

562   greater moisture source. Likewise, the increase over the western Indian Ocean is likely because

563   preindustrial Africa extends much further East than during the Eocene, again giving much less of a

564   moisture source during the PI (Figure 1a). Moreover, an examination of SST from the Eocene and PI

565   simulations (from each individual model and the MME) shows that these exposed regions of ocean

566   are characterised by warmer SSTs in the Eocene; for example, in the Indian Ocean absolute values are

567   up to 32°C in the Eocene MME compared to up to 28°C in the PI MME, thereby providing a greater

568   source of evaporation during the Eocene see (see Supplementary Material, Figure S2). Concerning

569   the drying over equatorial Eocene Africa, this is likely less related to the LSM (because the region

570   was land during both time periods), and more likely related to the change in vegetation (Figure 1c).

571   In these regions, at approximately 10°N, what is tropical rainforest during the PI is rather a mixture of

572   savanna, grassland and desert during the Eocene (Figure 1c) and would therefore likely explain the

573   reduction in precipitation because of the reduced evapotranspiration. Finally, although there is a large

574   increase in orographic heights (of over 1000 m) over southern Africa during the Eocene (Figure 1b

575   and Figure S1 in the Supplementary Material), this does not appear to be having a large impact on the

576   West African monsoon, with minimal precipitation differences further south (Figure 5a).

577
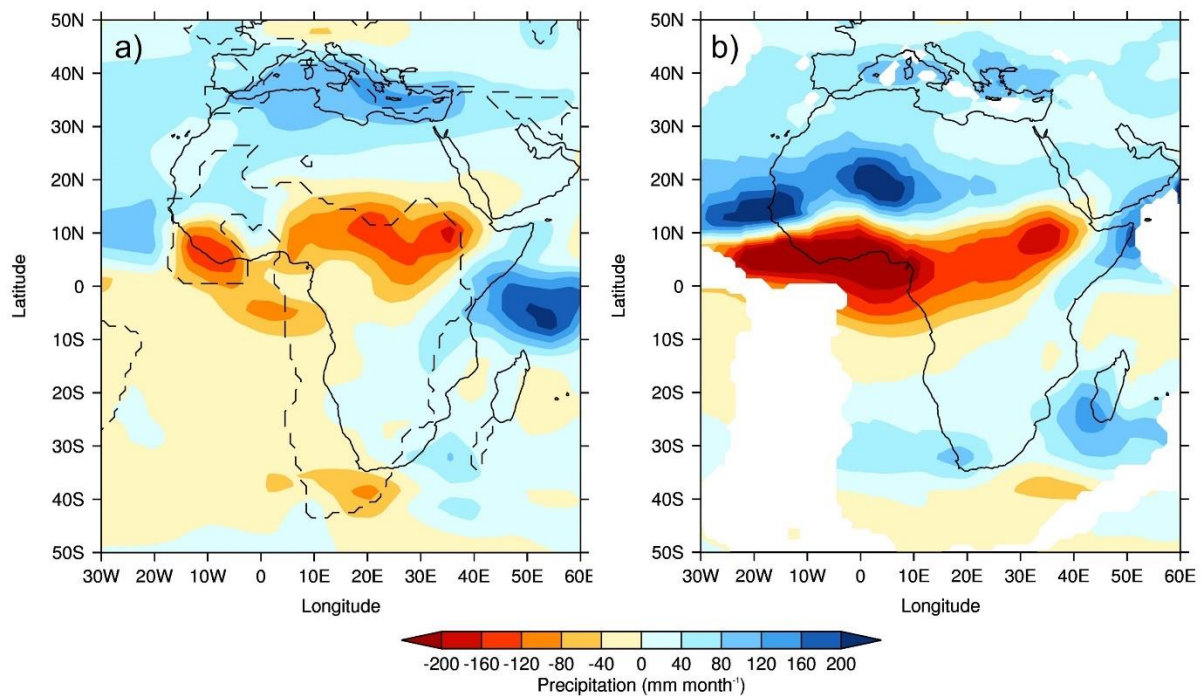
578   Figure 5 – JJA precipitation multi-model ensemble mean (MME) climatology differences (Eocene - PI) for the

579   1x CO_2 experiment (comprising the four models that conducted this experiment, in addition to the others

580   considered here: GFDL_CM2.1, HadCM3B_M2.1aN, HadCM3BL_M2.1aN and MIROC4m): a) Original (i.e.

581   unrotated) differences; b) Rotated differences i.e. Eocene precipitation rotated forward to where it is in the PI.

582   Note that in a), solid lines show the PI mask and dashed lines show the Eocene mask

583

584   However, a caveat of the above analysis is that, because of the plate rotation differences during the

585   Eocene, Figure 5a is showing precipitation anomalies that may simply be due to differing

586   geographical locations, rather than any change to the climate state. Therefore, Figure 5b shows the

587   same results, but this time with the Eocene precipitation rotated forwards (based on the rotations

21

588   supplied in the Herold *et al.* 2014 Supplementary Material) to where it is in the PI. However, despite

589   these rotational differences, the overall picture remains the same (i.e. increases in precipitation over

590   northern Africa and a decrease in precipitation over western and equatorial Africa) but much more

591   pronounced (Figure 5b). The increases and decreases in precipitation exceed 200 mm month^{-1} in

592   some places, suggesting a northward displacement of the Atlantic ITCZ; this difference between the

593   Eocene and the PI is in contrast to when the Eocene CO_2 experiments are compared with each other,

594   to assess the impact of increasing CO_2 (discussed further below in Section 3.2.3 and Section 4).

595

596   *3.2.3. Lower and higher CO_2 experiments: impact of CO_2*

597   To investigate the impact of increasing CO_2 on precipitation, when all other boundary conditions are

598   constant, the experiments have been divided into two samples, each containing a different number of

599   models going into the MME: i) "lower-level CO_2", namely the 1x, 2x and 3x experiments, comprising

600   four models (GFDL_CM2.1, HadCM3B_M2.1aN, HadCM3BL_M2.1aN and MIROC4m); and ii)

601   "higher-level CO_2", namely the 3x and 6x experiments, comprising two models (CESM1.2_CAM5

602   and GFDL_CM2.1); see Table 1. Note that the MMEs for the two 3x experiments are slightly

603   different because they contain a different number of models. Here, both absolute precipitation values

604   and anomalies are shown, where the anomalies are of a certain CO_2 experiment versus another CO_2

605   experiment, rather than Eocene versus PI.

606

607   The MME absolute precipitation and anomalies for the lower-level sample of CO_2 experiments, are

608   shown in Figure 6a. When the absolute values are considered (Figure 6a, top row), all experiments

609   show regions of precipitation maxima over the equatorial Atlantic (north of the Equator) and West

610   Africa. Over the same West African region as described above (20°W-15°E, 0-20°N, land points

611   only), mean JJA precipitation is 192 mm month^{-1}, 201 mm month^{-1} and 207 mm month^{-1} for the 1x, 2x

612   and 3x experiments, respectively, implying a small increase as CO_2 increases. This becomes more

613   evident when the anomalies are considered (Figure 6a, second row). If the 1x and 2x experiments are

614   compared, the largest change is over the equatorial Atlantic, with a small increase in precipitation of

615   up to 50 mm month^{-1} over the Equator and a decrease of over 50 mm month^{-1} further north, suggesting

616   a southward displacement of the Atlantic ITCZ. Precipitation is also increased over western Africa.

617   The same pattern is evident when the 1x and 3x experiments are compared, but more pronounced,

618   with both the increases and decreases approaching 100 mm month^{-1} in their respective areas.
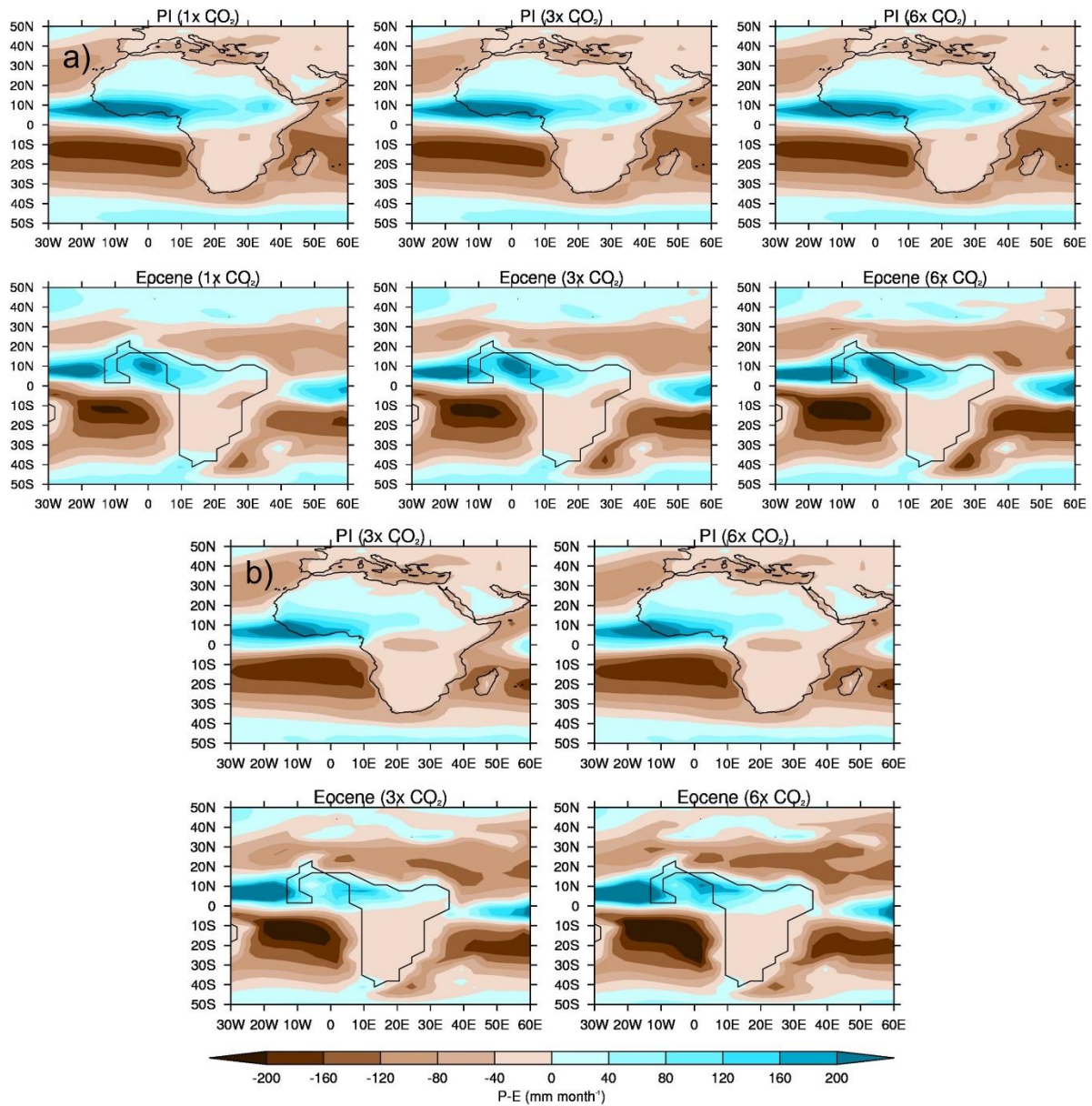
619

22
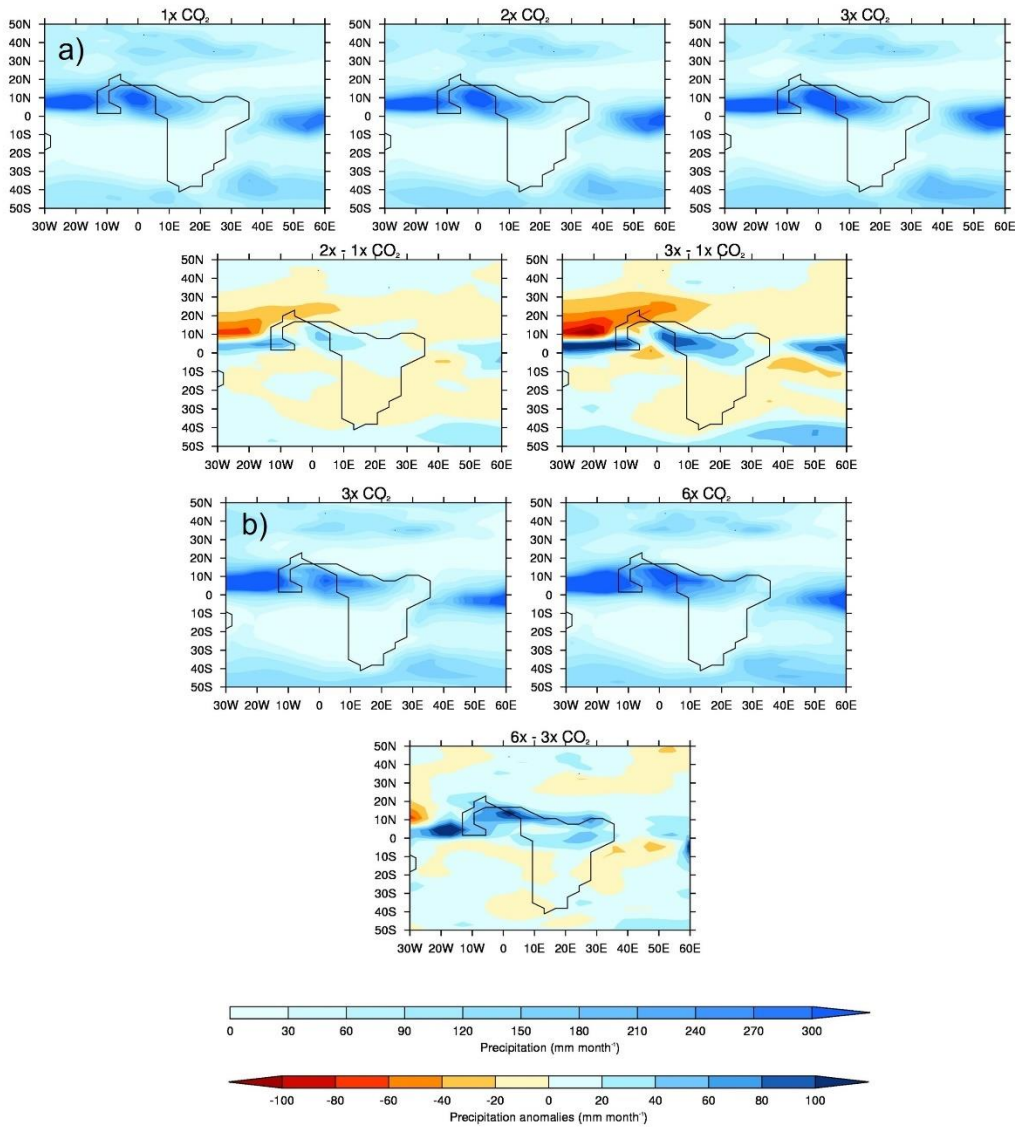
Figure 6 – JJA precipitation multi-model ensemble mean (MME) climatology absolutes and anomalies for the 1x, 2x, 3x and 6x CO$_2$ experiments, using both samples: a) Lower-level sample of CO$_2$ experiments (comprising the four models that conducted these: GFDL_CM2.1, HadCM3B_M2.1aN, HadCM3BL_M2.1aN and MIROC4m), absolutes (top row) and anomalies (second row); b) Higher-level sample of CO$_2$ experiments (comprising the two models that conducted these: CESM1.2_CAM5 and GFDL_CM2.1), absolutes (top row) and anomalies (second row)

The MME absolute precipitation and anomalies for the higher-level sample of CO$_2$ experiments are shown in Figure 6b. When the absolute values are considered (Figure 6b, top row), the region of precipitation maxima in the equatorial Atlantic is larger in the 6x experiment. Over the same West African region, mean JJA precipitation is 186 mm month^{-1} and 232 mm month^{-1} for the 3x and 6x experiments, respectively, implying a large mean increase as CO$_2$ increases, and this is further confirmed when the anomalies are considered (Figure 6b, second row). Precipitation increases of over 100 mm month^{-1} are shown over the equatorial Atlantic (north of the Equator) and West Africa

635   in the 6x relative to the 3x experiment, but the large region of drying seen at the lower levels of CO_2

636   is less evident (Figure 6b, second row). This suggests that, whilst West African precipitation is still

637   (and more so here) enhanced as CO_2 rises, it is perhaps less related to Atlantic ITCZ displacement and

638   more related to an increase in south-westerly flow (discussed below).

639

640   **3.3. Physical mechanisms behind the precipitation response**

641   Here the focus is on the possible dynamic and thermodynamic mechanisms causing the observed

642   precipitation responses, again using the MME absolute values and anomalies from the aforementioned

643   lower-and higher level samples of CO_2 experiments.

644

645   The MME absolute 1.5 m surface air temperature (SAT) and anomalies for the lower- and higher-

646   level sample of CO_2 experiments are shown in Figure 7. In line with general understanding there is a

647   clear increase in absolute SAT, everywhere, as the CO_2 increases, with the largest signal (of up to

648   40°C in the 3x experiment) occurring over the main landmass of central and northern Africa (Figure

649   7a, top row). This is more obvious when the anomalies are considered, although the largest increases

650   are occurring further south (Figure 7a, second row). This is even more pronounced in the higher-level

651   sample of CO_2 experiments (Figure 7b), and in all experiments the largest increase in SAT, either

652   between the 3x and 1x experiments or the 6x and 3x the experiments, is occurring over southern

653   Africa, away from the largest precipitation changes discussed above. The Precipitation - Evaporation

654   (P-E) balance (Figure 8) is positive over West Africa in all experiments regardless of sample,

655   corresponding well with the region of increased precipitation (Figure 6), as does cloud cover which is

656   also increasing with CO_2 over these regions (not shown). Further south, over the Atlantic, the balance

657   is negative implying increased evaporation corresponding to the increased oceanic SAT. Concerning

658   low level circulation, as shown by 850 mb vector winds (Figure 9), when the anomalies are

659   considered (and in particular the 3x versus 1x), there is a small (of up to 5 ms^{-1}) increase in northerly

660   and westerly winds (i.e. clockwise flow) in the equatorial Atlantic north of the Equator (Figure 9a,

661   second row). However, in the higher-level CO_2 sample (and in particular the anomalies of 6x versus

662   3x, Figure 9b, second row), this increase in anticyclonic flow is less evident and is instead replaced by

663   a widespread area of increased southwesterly flow across most of the equatorial Atlantic and central

664   Africa. For SAT, P-E and 850 vector winds from each individual model, rather than the MME, see

665   the Supplementary Material (Figure S3a, b, and c, respectively); here, similar to Figure 4, there is no

666   obvious linear change in either P-E or low level circulation as CO_2 increases, but a clear increase in

667   SAT from all models, in line with current understanding (Figure S3a).

668

Figure 7 – Same as Figure 6 but for JJA 1.5 m surface air temperature

Figure 8 – JJA P-E multi-model ensemble mean (MME) climatology absolutes for the 1x, 2x, 3x and 6x CO_2 experiments, using both samples: a) Lower-level sample of CO_2 experiments (comprising the four models that conducted these: GFDL_CM2.1, HadCM3B_M2.1aN, HadCM3BL_M2.1aN and MIROC4m), PI (top row) and Eocene (bottom row); b) Higher-level sample of CO_2 experiments (comprising the two models that conducted these: CESM1.2_CAM5 and GFDL_CM2.1), PI (top row) and Eocene (bottom row). Note that the PI panels are identical in each sample because they contain the same models, but are simply replicated here for ease of comparison
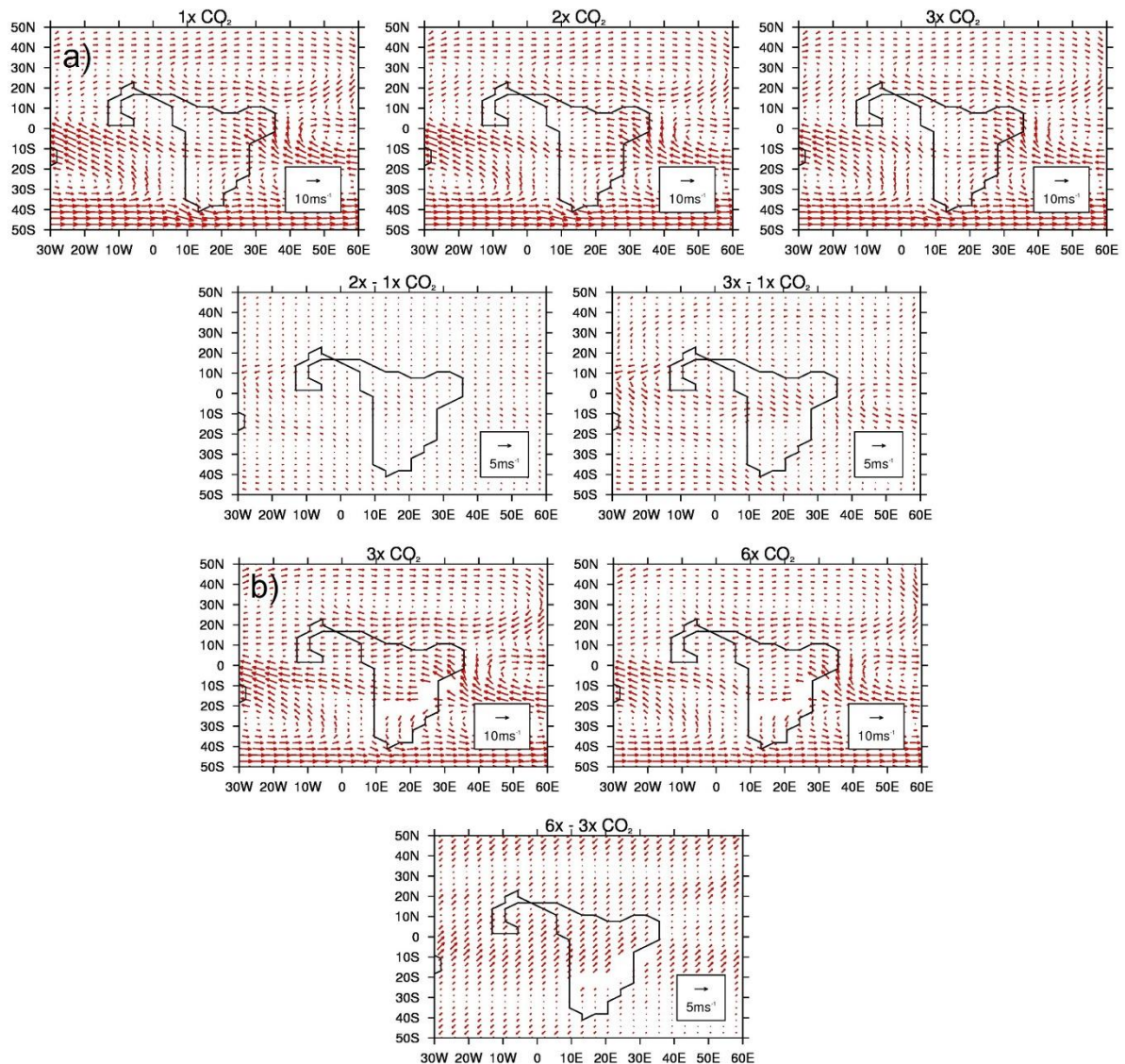
Figure 9 – Same as Figure 6 but for JJA 850 mb wind

3.4. DeepMIP models' Eocene simulations versus proxy data

In this final section, the focus is on comparing precipitation from selected DeepMIP Eocene
simulations (using the MME from the same two samples as discussed above) with newly-available
precipitation reconstructions (described in Section 2.3.2). Before the results are presented, however,
several sources of uncertainty in the proxies and models must be noted, aside from analytical
uncertainty that is expressed in the reconstructed confidence intervals. Firstly, the fossil plant
assemblages analysed here have broad age constraints. Palaeofloral assemblages may capture a
snapshot within those age constraints that deviated climatically from the average climatic conditions
of a specific age that the model was calibrated on. In addition, fossil plant assemblages tend to
preserve better in wetter climates, with drier climates lacking the water bodies needed to preserve
plant fossils. Secondly, the DeepMIP models are calibrated on atmospheric CO_2 proxy
reconstructions to cover the uncertainty of the entire Eocene; the lower CO_2 levels may be more

27

696   representative of the late Eocene, but that was not the purpose or interpretation when it came to

697   deciding the experiments. Independent proxies within those ages produce widely variable

698   atmospheric CO_2 reconstructions (e.g. Rae *et al*. 2021), with <500 ppmv from some palaeosol and

699   stomatal reconstructions (Beerling *et al*. 2009; Hyland *et al*. 2013) to >2000 ppmv from boron

700   isotopes and alkenone δ13C (e.g. Bijl *et al*. 2010; Anagnostou *et al*. 2020). It should be noted,

701   however, that there is high uncertainty in these reconstructions; see Hollis *et al*. 2019 for a full

702   discussion. For example, based on a variety of reconstructions compiled as part of the Palaeo-CO_2

703   project (including phytoplankton, boron proxies, leaf gas exchange, liverworts and nahcolite),

704   atmospheric CO_2 during 55-50 Ma ranges from 500-2000 ppmv (Anagnostou *et al*. 2020, Hollis *et al*.

705   2019, Westerhold *et al*. 2020). Potentially, these differences in reconstructed atmospheric CO_2 reflect

706   transient climate states (e.g. Reichgelt *et al*. 2016), but regardless, the disagreement between proxy

707   reconstructions makes it problematic to associate a single atmospheric CO_2 level for model-data

708   comparison (Hollis *et al*. 2019). Lastly, a major source of uncertainty is the paucity of proxy data

709   across Africa; as mentioned above, even today there is a lack of long-term climate data over much of

710   Africa, and the same is true for palaeofloras. This sparsity, therefore, is likely responsible for some of

711   the results discussed below.

712

713   With these caveats in mind, MME MAP at each of the individual locations is shown in Figure 10,

714   ordered according to the reconstructions' values, including uncertainty estimates for the

715   reconstructions (as measured by +/- 1 standard deviation for the locations in Mahenge, Tanzania and

716   the 95% confidence interval for the other 11 locations; see Table 2 for details). The approximate

717   geographical locations can be seen in the Supplementary Material (Figure S4). Firstly it is worth

718   noting that for the majority of reconstructions, uncertainty is high, with a range of up to +/- 1000 mm

719   yr⁻¹ at some of the locations such as Mwadui, Tanzania (Figure 10). Secondly, whether or not the

720   CO_2 experiments over- or underestimate MAP appears to depend heavily on geographical location,

721   with none of the CO_2 experiments (not even the 6x experiment) reproducing the precipitation amounts

722   of the proxy reconstructions in some locations, such as Koningsnaas, South Africa, Okigwe, Nigeria

723   or Tano, Ghana (Figure 10). Elsewhere, the simulations lie within the uncertainty range of the

724   reconstructions (such as Sagamu or Bende-Umuahia, both in Nigeria), and yet in other places (such as

725   across Kwakwa, Cameroon, and all of the locations at Mahenge, Tanzania) all of the simulations are

726   too wet, by between ~760-1040 mm year⁻¹ depending on location and CO_2 experiment (Figure 10).
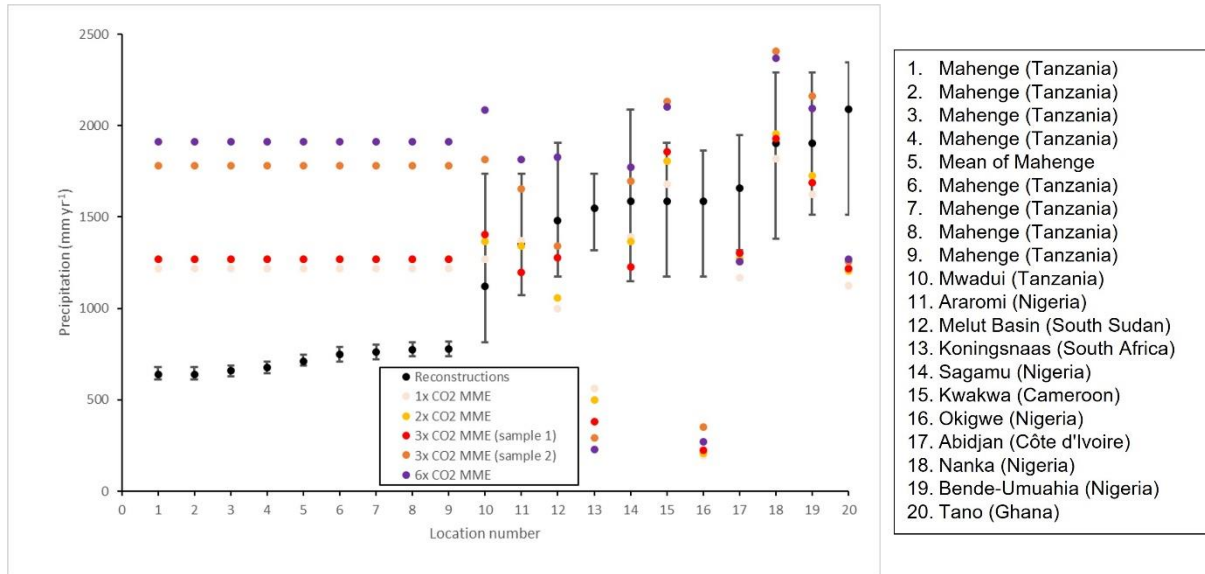
727

Figure 10 – Annual mean precipitation from reconstructions (black) and CO_2 experiments multi-model ensemble mean (MME, colours) at each individual location. Uncertainty in reconstructions is measured by 95% confidence interval for all sites except Mahenge, where they show +/- 1 standard deviation. Locations have been ordered according to the reconstructions' values, lowest to highest. Note that locations 1-4 and 6-8 are all in the same location, but from different stages during the Lutetian (~41-47 Ma), and so have been re-sampled and averaged into one overall mean (location 5)

Spatially, MME MAP is shown in Figure 11 (see Figure S5 in the Supplementary Material for each individual model), showing the uncertainty estimates as concentric circles. As already discussed, the simulations' precipitation is clearly too high or too low compared to proxy reconstructions in different parts of Africa. Qualitatively, in very general terms all of the CO_2 experiments are showing wetter conditions over Western Eocene Africa (relative to elsewhere), agreeing with Figure 10 where in many of these locations the models are either within, or at the higher end of, the reconstructions' uncertainty ranges (Figure 11). Importantly, simulated precipitation over West Africa appears to be increasing as the CO_2 concentration increases and, in particular for the 6x experiment (Figure 11e), in this region simulated precipitation exceeds even the upper range of uncertainty of the reconstructions.

745

746   Figure 11 – Annual mean precipitation from reconstructions (circles) and CO_2 experiments multi-model

747   ensemble mean (MME, background gridded data): a) 1x; b) 2x; c) 3x (lower-level CO_2 sample); d) 3x (higher

748   level CO_2 sample); e) 6x. Concentric circles show 95% confidence interval for all sites except Mahenge, where

749   they show +/- 1 standard deviation: outer circle = lower range (or -1 standard deviation), middle circle = average

750   (or, for Mahenge, mode) and inner circle = upper range (or +1 standard deviation).   Reconstructions have been

751   rotated forwards to where they are in the PI. Solid lines show the PI mask and dashed lines show the Eocene

752   mask. Note that, using the common spatial resolution of the MME, 3 reconstructions are all in the same location

753   in West Africa (even though they are in different locations in reality); here, therefore, only the top-most

754   reconstruction is shown

755

756   Quantitatively, the root mean squared error (RMSE) between each model (as well as the MME) and

757   the reconstructions at every location is shown in Table 3 and, similar to the anomalies from each

758   model as discussed above, there is no clear relationship between changing CO_2 and a better match to

759   the reconstructions. Most models suggest a better fit to the reconstructions at lower levels of CO_2,

760   such as CESM1.2_CAM5 where there is a general increase in RMSE as the CO_2 increases; however,

761   this is not the case for every model, with for example GFDL_CM2.1 showing a better fit with

762   reconstructions at 2x and 4x CO_2, rather than higher or lower levels (Table 3). For many of the

763   models and the MME, the 3x CO_2 experiments are showing the least fit with reconstructions. The

764   MME, from the lower-level (but not in the higher-level) CO_2 sample, agrees with this conclusion that

30

lower CO_2 is giving a slightly better match to the reconstructions, with RMSE values of 758 mm year^{-1}, 831 mm year^{-1}, 1385 mm year^{-1}, 889 mm year^{-1} and 839 mm year^{-1} for the 1x, 2x, 3x (lower-level CO_2 sample), 3x (higher-level CO_2 sample) and 6x experiments, respectively (Table 3).

	1x CO$_2$	1.5x CO$_2$	2x CO$_2$	3x CO$_2$	4x CO$_2$	6x CO$_2$	9x CO$_2$
CESM1.2_CAM5	681			750		704	822
COSMOS-landveg_r2413	699			1424	713		
GFDL_CM2.1	803		762	1027	786	975	
HadCM3B_M2.1aN	796		884	1988			
HadCM3BL_M2.1aN	816		1018	1742			
INM-CM4-8						966	
IPSLCM5A2		744		669			
MIROC4m	614		662	785			
NorESM1_F			1149		1522		
MME (lower-level CO$_2$ sample)	758		831	1385			
MME (higher-level CO$_2$ sample)				889		839	

Table 3 - Root Mean Squared Error (RMSE) for mean annual precipitation (MAP) between each model (and multi-model ensemble mean, MME, using both samples) and reconstructions, for each CO_2 experiment

4. DISCUSSION AND CONCLUSIONS

This study has investigated African precipitation during the early Eocene, as simulated by the DeepMIP models. This study is novel, because it investigates the relatively little-studied subject of African hydroclimate during the early Eocene. The results of this study have been divided into four separate sections, corresponding to the four questions posed in Section 1. Firstly, in Section 3.1 the DeepMIP models' PI simulations have been compared to satellite-derived estimates of precipitation, to ascertain how well the models are able to reproduce African precipitation under 'modern' conditions (please see Section 2.3.1 for a discussion of the caveat that here the term 'modern' is actually a combination of both pre-industrial and 20th-21st century). Secondly, in Section 3.2 the DeepMIP models' Eocene simulations have been compared to both the PI simulations and each other, to investigate the impact of non-CO_2 components (i.e. other boundary condition changes, such as to the LSM) and CO_2 components (i.e. increasing CO_2) on African precipitation. Thirdly, in Section 3.3 the CO_2 driven response has been investigated further by looking at a number of dynamic and thermodynamic fields simulated by the models, to ascertain possible physical mechanisms behind the observed precipitation response. Lastly, in Section 3.4 the DeepMIP models' Eocene simulations have been compared to newly-available proxy data, to indicate how well the models agree with current best precipitation estimates from the Eocene.

790

The comparison between the DeepMIP PI simulations and modern observations (from TAMSAT) suggest that individual models are both underestimating or overestimating the spatial patterns of African precipitation; this is consistent with Monerie *et al*. (2020), who analysed a number of historical simulations from both CMIP5 and CMIP6 and found that the models' ability to reproduce observations was firstly model dependent and secondly geographically dependent, with many models underestimating precipitation over the Sahel and overestimating it over the Guinea coast and tropical Atlantic. However, here the MME is reducing these biases and is showing the best agreement with TAMSAT in terms of precipitation spatial patterns, highlighting the utility of the MME as a best estimate of the actual precipitation. This has been found elsewhere, such as by Ayugi *et al*. (2021) who looked at East African precipitation in both CMIP5 and CMIP6 models and again found a better performance of the MME relative to individual models, due to systematic errors in individual models being cancelled out. Moreover, Rougier *et al*. (2013) show that it is actually a statistical property of this type of analysis that the ensemble mean will always provide the best match to the data e.g. have the lowest RMSE. Concerning the latitudinal extent and seasonal timings of African precipitation, most models show a much wider (latitudinally) West African rain belt compared to TAMSAT and are not reproducing the rapid drop-off in precipitation near the Equator or north of 15°N. This is somewhat in contrast to Monerie *et al*. (2020), who noted that the majority of CMIP5 and CMIP6 models did not have the monsoon extending far enough to the north and were instead showing a southward displacement of precipitation maxima, relative to observations; however, that particular study used the models' historical simulations (as well as a different MME), not pre-industrial as shown here, which may explain the discrepancy. Outside of the JJA West African monsoon season most models are too wet, but within the monsoon season the results suggest that the drier models (i.e. those underestimating West African precipitation) are closer to modern observations than those that are too wet (i.e. overestimating West African precipitation).

The comparison between the DeepMIP Eocene simulations and the PI suggests that, when all individual models are considered separately, there is no obvious wetting or drying trend (relative to the PI) as the CO_2 increases. This is another reason to focus on the MME, which allows easier interpretation as the large model spread is removed. Concerning the non-CO_2 component of precipitation change (i.e. the impact of other boundary conditions when CO_2 is kept at PI levels), the results suggest that changes to the LSM may be responsible for the increases in precipitation (relative to the PI) to the north of Eocene Africa and the western Indian Ocean, given that these are 'newly exposed' regions of ocean in the Eocene, thereby providing a larger moisture source. In contrast, it is likely that changes in vegetation are responsible for the region of drying (relative to the PI) over equatorial Eocene Africa, because regions of tropical rainforest during the PI were instead savanna and desert during the Eocene, thereby reducing the amount of evapotranspiration and evaporation. It

827 should be noted, though, that validation of the Eocene vegetation over certain regions of Africa was

828 not possible when creating this boundary condition (Herold *et al.* 2014), therefore there is a level of

829 uncertainty here. When the Eocene precipitation is rotated forwards in time to where it is in the PI, a

830 similar pattern is shown but is more pronounced, and suggests a northward displacement of the

831 primary rain belt (relative to today), which is consistent with previous work (e.g. Carmichael *et al.*

832 2016). However, this is in contrast to when CO_2 is increased in the Eocene simulations. Concerning

833 this CO_2 component of precipitation change, at the lower levels of increased CO_2 (such as 2x and 3x

834 that of the PI) precipitation over the equatorial Atlantic and West Africa appears to be increasing in

835 response to rising CO_2, with the concomitant decrease in precipitation north of the equator suggesting

836 a possible displacement of the Atlantic ITCZ towards the south. This therefore suggests that the

837 boundary condition changes imposed for the Eocene are resulting in a northward displacement of the

838 primary rain belt, but increasing CO_2 (with the same boundary conditions) is resulting in a southward

839 displacement of the primary rain belt. At even higher levels of CO_2 (such as 6x that of the PI),

840 precipitation over West Africa is more enhanced relative to the lower levels, but the region of drying

841 is less evident. The enhancement of Northern Hemisphere summer West African precipitation at the

842 highest levels of CO_2 is again consistent with previous work, such as that of Carmichael *et al.* (2016)

843 who showed a generally more intense hydrological cycle at higher CO_2 levels and that of Carmichael

844 *et al.* (2018) who demonstrated an increase in precipitation extremes over tropical Africa at higher

845 CO_2 levels.

846

847 Consistent with Carmichael *et al.* (2016), the precipitation increases over West Africa as CO_2

848 concentrations rise are associated with increased SAT, a strongly positive the P-E balance and cloud

849 cover increases and, concerning temperature, as such are consistent with the idea that a generally

850 warmer world results in a generally wetter world; the 'wet-gets-wetter and dry-gets-drier' hypothesis

851 (e.g. Held and Soden 2006). However, the largest increases in SAT shown here are over southern

852 Africa, not where the largest precipitation increases are seen, suggesting factors other than a generally

853 warming world (i.e. dynamical changes) are responsible for the localised precipitation response. Both

854 the region of enhanced precipitation over West Africa, and the region of drying in the equatorial

855 Atlantic around 10°N, may be explained by low-level circulation changes. Up to 3x that of the PI

856 CO_2, clockwise low-level circulation increases with CO_2, drawing in more moisture from the

857 equatorial Atlantic and causing a relative drying further north, hence the appearance of a southward

858 displacement of the Atlantic ITCZ. At higher levels of CO_2, however, where increases in West

859 African precipitation are shown but the region of drying around 10°N is not, the increased clockwise

860 low-level circulation is replaced by increased south-westerly flow; here, therefore, precipitation is

861 being enhanced by more moisture being drawn in by this south-westerly flow from the warm South

862 Atlantic.

863

864   Lastly, the results from the model-data comparison suggests that whether the Eocene simulations

865   (regardless of CO_2 experiment) over- or underestimate African precipitation is highly geographically

866   dependent, with some of the CO_2 experiments at some of the locations lying within the uncertainty

867   range of the reconstructions but others being too wet or too dry. There is some suggestion of a

868   latitudinal relationship, with the simulations overestimating precipitation near the Equator and

869   underestimating precipitation in high latitude regions, such as South Africa; this latter point is

870   consistent with the findings of Carmichael *et al*. (2016). Whether the models are considered

871   independently or whether the MME is used, the results suggest a marginally better fit with the

872   reconstructions at lower levels of CO_2, and this is in contrast (indirectly) to the findings of Carmichael

873   *et al*. (2016) who suggested the warmest models in the regions of increased precipitation best matched

874   the data; it should be noted, however, that this was a global study. There is no evidence for this here,

875   and indeed the finding of a better match at lower levels of CO_2 is in contrast to that of Reichgelt *et al*.

876   (2021, in prep) who focused on Australia and found that the higher, 6x CO_2 experiment was the best

877   match to reconstructions. However, given the uncertainties associated with both the reconstructions

878   (discussed above) and the boundary conditions used to force the models, it is difficult to draw firm

879   conclusions from a model-data comparison of this type. Moreover, a particularly big problem here is

880   that, despite the newly-compiled reconstructions presented here, there is still a lack of data across

881   Africa, hindering any firm conclusions.

882

883   In conclusion, therefore, this study has shown that the DeepMIP models are able to approximately

884   reproduce the modern African precipitation and, in response to rising CO_2, suggest an enhancement of

885   precipitation in this region associated with increasing temperatures and changes to low-level

886   circulation. At very high levels of CO_2 the models may be too wet, relative to reconstructions.

887   However, this might be because the NLR proxy approach has difficulty generating MAP values above

888   modern, or connected to the relatively few data points within the reconstructions. Using the MME

889   provides the clearest suggestion of this, but the large amount of model spread means that when

890   individual models are considered, either relative to their corresponding PI simulations or

891   reconstructions, no clear relationship is shown.

892

893   **DATA AVAILABILITY**

894   TAMSAT data are publicly available to download at https://www.tamsat.org.uk/. The

895   palaeobotanical precipitation estimates compiled here are available as a spreadsheet included in the

896   Supplementary Material. The DeepMIP PI and Eocene simulations are available by following the

897   instructions at https://www.deepmip.org/data-eocene/.

898

899

900

981 precipitation rotated forward to where it is in the PI. Note that in a), solid lines show the PI mask and

982 dashed lines show the Eocene mask

983

984 Figure 6 – JJA precipitation multi-model ensemble mean (MME) climatology absolutes and

985 anomalies for the 1x, 2x, 3x and 6x CO_2 experiments, using both samples: a) Lower-level sample of

986 CO_2 experiments (comprising the four models that conducted these: GFDL_CM2.1,

987 HadCM3B_M2.1aN, HadCM3BL_M2.1aN and MIROC4m), absolutes (top row) and anomalies

988 (second row); b) Higher-level sample of CO_2 experiments (comprising the two models that conducted

989 these: CESM1.2_CAM5 and GFDL_CM2.1), absolutes (top row) and anomalies (second row)

990

991 Figure 7 – Same as Figure 6 but for JJA 1.5 m surface air temperature

992

993 Figure 8 – JJA P-E multi-model ensemble mean (MME) climatology absolutes for the 1x, 2x, 3x and

994 6x CO_2 experiments, using both samples: a) Lower-level sample of CO_2 experiments (comprising the

995 four models that conducted these: GFDL_CM2.1, HadCM3B_M2.1aN, HadCM3BL_M2.1aN and

996 MIROC4m), PI (top row) and Eocene (bottom row); b) Higher-level sample of CO_2 experiments

997 (comprising the two models that conducted these: CESM1.2_CAM5 and GFDL_CM2.1), PI (top row)

998 and Eocene (bottom row). Note that the PI panels are identical in each sample because they contain

999 the same models, but are simply replicated here for ease of comparison

1000

1001 Figure 9 – Same as Figure 6 but for JJA 850 mb wind

1002

1003 Figure 10 – Annual mean precipitation from reconstructions (black) and CO_2 experiments multi-

1004 model ensemble mean (MME, colours) at each individual location. Uncertainty in reconstructions is

1005 measured by 95% confidence interval for all sites except Mahenge, where they show +/- 1 standard

1006 deviation. Locations have been ordered according to the reconstructions' values, lowest to highest.

1007 Note that locations 1-4 and 6-8 are all in the same location, but from different stages during the

1008 Lutetian (~41-47 Ma), and so have been re-sampled and averaged into one overall mean (location 5)

1009

1010 Figure 11 – Annual mean precipitation from reconstructions (circles) and CO_2 experiments multi-

1011 model ensemble mean (MME, background gridded data): a) 1x; b) 2x; c) 3x (lower-level CO_2

1012 sample); d) 3x (higher level CO_2 sample); e) 6x. Concentric circles show 95% confidence interval for

1013 all sites except Mahenge, where they show +/- 1 standard deviation: outer circle = lower range (or -1

1014 standard deviation), middle circle = average (or, for Mahenge, mode) and inner circle = upper range

1015 (or +1 standard deviation). Reconstructions have been rotated forwards to where they are in the PI.

1016 Solid lines show the PI mask and dashed lines show the Eocene mask. Note that, using the common

1017 spatial resolution of the MME, 3 reconstructions are all in the same location in West Africa (even

though they are in different locations in reality); here, therefore, only the top-most reconstruction is
shown

LIST OF SUPPLEMENTARY TABLES/FIGURES

1054   all in the same location in West Africa (even though they are in different locations in reality); here,

1055   therefore, only the top-most reconstruction is shown

REFERENCES

Adeonipekun, P. A., Ehinola, O. A., Yussuph, I. A., Toluhi, A. and Oyelami, A.: Bio-sequence stratigraphy of Shagamu Quarry outcrop, Benin Basin, southwestern Nigeria, World Applied Sciences Journal, 18, 91-106, DOI: 10.5829/idosi.wasj.2012.18.01.3572, 2012.

Anagnostou, E., John, E. H., Babila, T. L., Sexton, P. F., Ridgwell, A., Lunt, D. J., Pearson, P. N., Chalk, T. B., Pancost, R. D. and Foster, G. L.: Proxy evidence for state-dependence of climate sensitivity in the Eocene greenhouse, Nature Communications, 11(4436), https://doi.org/10.1038/s41467-020-17887-x, 2020.

Anagnostou, E., John, E. H., Edgar, K. M., Foster, G. L., Ridgwell, A., Inglis, G. N., Pancost, R. D., Lunt D. J. and Pearson, P. N.: Changing atmospheric CO2 concentration was the primary driver of early Cenozoic climate, Nature, 533, 380–384, https://doi.org/10.1038/nature17423, 2016.

Arakawa, A. and Schubert, W. H.: Interactions of cumulus cloud ensemble with the large-scale environment. Part I, J. Atmos. Sci., 31, 671-701, https://doi.org/10.1175/1520-0469(1974)031<0674:IOACCE>2.0.CO;2, 1974.

Arias, P. A., Bellouin, N., Coppola, E. et al.: Technical Summary. In Climate Change 2021: The Physical Science Basis. Contribution of Working Group I to the Sixth Assessment Report of the Intergovernmental Panel on Climate Change [Masson-Delmotte, V., Zhai, P., Pirani, A., Connors, S. L., Péan, C., Berger, S., Caud, N., Chen, Y., Goldfarb, L., Gomis, M. I., Huang, M., Leitzell, K., Lonnoy, E., Matthews, J. B. R., Maycock, T. K., Waterfield, T., Yelekçi, O., Yu, R. and Zhou, B. (eds.)], Cambridge University Press, In Press, https://www.ipcc.ch/report/ar6/wg1/#TS, 2021.

Atta-Peters, D. and Salami, M. B.: Late Cretaceous to early Tertiary pollen grains from offshore Tano Basin, southwestern Ghana, Revista Española de Micropaleontologia, 36(3), 451-465, https://dialnet.unirioja.es/servlet/articulo?codigo=1070295, 2004.

Ayugi, B., Zhihong, J., Zhu, H., Ngoma, H., Babaousmail, H., Rizwan, K. and Dike, V.: Comparison of CMIP6 and CMIP5 models in simulating mean and extreme precipitation over East Africa, Int. J. Clim., https://doi.org/10.1002/joc.7207, 2021.

Beerling, D. J., Fox, A. and Anderson, C. W.: Quantitative uncertainty analyses of ancient atmospheric CO_2 estimates from fossil leaves, AJS, 309(9), 775-787, DOI: https://doi.org/10.2475/09.2009.01, 2009.

1093 Betts, K.: A new convective adjustment scheme. Part 1. Observational and theoretical basis, Q. J.

1094 R.Meteorol. Soc. 112, 677-691, https://doi.org/10.1002/qj.49711247307, 1986.

1095

1096 Bijl, P. K., Houben, A. J. P., Schouten, S., Bohaty, S. M., Sluijs, A., Reichart, G.-J., Sinninghe

1097 Damsté J. S. and Brinkhuis, H.: Transient middle Eocene atmospheric CO_2 and temperature

1098 variations, Science, 330(6005), 819-821, DOI: 10.1126/science.1193654, 2010.

1099

1100 Bony, S. and Emanuel, K. A.: A parameterization of the cloudiness associated with cumulus

1101 convection; evaluation using TOGA COARE data, J. Atmos. Sci., 58(21), 3158-3183,

1102 https://doi.org/10.1175/1520-0469(2001)058<3158:APOTCA>2.0.CO;2, 2001.

1103

1104 Braconnot, P., Harrison, S. P., Otto-Bliesner, B. L., Abe-Ouchi, A., Jungclaus, J. and Peterchmitt, J.-

1105 Y.: The palaeoclimate modelling intercomparison project contribution to CMIP5, CLIVAR Exch.

1106 Newsl, 56, 15–19, 2011.

1107

1108 Braconnot, P., Otto-Bliesner, B., Harrison, S., Joussaume, S., Peterchmitt, J.-Y., Abe-Ouchi, A.,

1109 Crucifix, M., Driesschaert, E., Fichefet, Th., Hewitt, C. D., Kageyama, M., Kitoh, A., Laîné, A.,

1110 Loutre, M.-F., Marti, O., Merkel, U., Ramstein, G., Valdes, P., Weber, S. L., Yu, Y., and Zhao, Y.:

1111 Results of PMIP2 coupled simulations of the Mid-Holocene and Last Glacial Maximum – Part 1:

1112 experiments and large-scale features, Clim. Past, 3, 261-277, https://doi.org/10.5194/cp-3-261-2007,

1113 2007.

1114

1115 Bushell, A. C.: Chapter 2 Understanding the Unified Model (Section 2.1.1), in Matthews, D.: Unified

1116 Model User Guide, http://www.ukscience.org/_Media/UM_User_Guide.pdf, Accessed 22/9/21, 1998.

1117

1118 Cantrill, D. J., Bamford, M. K., Wagstaff, B. E. and Sauquet, H.: Early Eocene fossil plants from the

1119 Mwadui kimberlite pipe, Tanzania, Review of Palaeobotany and Palynology, 196, 19-35, DOI:

1120 10.1016/j.revpalbo.2013.04.002, 2013.

1121

1122 Carmichael, M. J., Lunt, D. J., Huber, M., Heinemann, M., Kiehl, J., LeGrande, A., Loptson, C. A.,

1123 Roberts, C. D., Sagoo, N., Shields, C., Valdes, P. J., Winguth, A., Winguth, C. and Pancost, R. D.: A

1124 model-model and data-data comparison for the early Eocene hydrological cycle, Clim. Past, 12, 455-

1125 481, doi:10.5194/cp-12-455-2016, 2016.

1126

1127 Carmichael, M. J., Pancost, R. D. and Lunt D. J.: Changes in the occurrence of extreme precipitation

1128 events at the Paleocene–Eocene thermal maximum, Earth Planet. Sci. Lett., 501, 24-36,

1129 https://doi.org/10.1016/j.epsl.2018.08.005, 2018.

1130

1131 Chan, W.-L., Abe-Ouchi, A. and Ohgaito, R.: Simulating the mid- Pliocene climate with the MIROC

1132 general circulation model: experimental design and initial results, Geosci. Model Dev., 4, 1035-1049,

1133 https://doi.org/10.5194/gmd-4-1035-2011, 2011.

1134

1135 Chiaghanam, O. I., Chiadikobi, K.C., Oguanya, C.E., Ikegwuonu, O.N., Nwokeabia, C.N.:

1136 Palynological and Paleoenvironmental Study of Paleogene in Bende - Umuahia, Niger Delta Basin,

1137 Nigeria, Journal of Environment and Earth Science, 7, 97-107, ISSN 2225-0948, 2017.

1138

1139 Cox, P. M.: A primitive equation, 3-dimensional model of the ocean, GFDL Ocean Group Technical

1140 Report No. 1, Geophysical Fluid Dynamics Laboratory, Princeton, New Jersey, 1984.

1141

1142 Cox, P. M., Betts, R. A., Bunton, C. B., Essery, R. L. H., Rowntree, P. R. & Smith, J.: The impact of

1143 new land surface physics on the GCM simulation of climate and climate sensitivity. Clim. Dyn.,

1144 15(3), 183-203. https://doi.org/10.1007/s003820050276, 1999.

1145

1146 de Villiers, S. E.: The palynology of Tertiary sediments from a palaeochannel in Namaqualand,

1147 Doctor of Philosophy thesis, Faculty of Science, University of Witwatersrand, Johannesburg, 100 pp.,

1148 1997.

1149

1150 Delworth, T. L., Broccoli, A. J., Rosati, A., Stouffer, R. J., Balaji, V., Beesley, J. A., Cooke,W. F.,

1151 Dixon, K.W., Dunne, J., Dunne, K. A., Durachta, J. W., Findell, K. L., Ginoux, P., Gnanadesikan, A.,

1152 Gordon, C. T., Griffies, S. M., Gudgel, R., Harrison, M. J., Held, I. M., Hemler, R. S., Horowitz, L.

1153 W., Klein, S. A., Knutson, T. R., Kushner, P. J., Langenhorst, A. R., Lee, H.-C., Lin, S.-J., Lu, J.,

1154 Malyshev, S. L., Milly, P. C. D., Ramaswamy, V., Russell, J., Schwarzkopf, M. D., Shevliakova, E.,

1155 Sirutis, J. J., Spelman, M. J., Stern, W. F., Winton, M., Wittenberg, A. T., Wyman, B., Zeng, F. and

1156 Zhang, R.: GFDL's CM2 Global Coupled Climate Models. Part I: Formulation and Simulation

1157 Characteristics, J. Climate, 19, 643–674, https://doi.org/10.1175/JCLI3629.1, 2006.

1158

1159 Dufresne, J.-L., Foujols, M.-A., Denvil, S., Caubel, A., Marti, O., Aumont, O., Balkanski, Y., Bekki,

1160 S., Bellenger, H., Benshila, R., Bony, S., Bopp, L., Braconnot, P., Brockmann, P., Cadule, P., Cheruy,

1161 F., Codron, F., Cozic, A., Cugnet, D., de Noblet, N., Duvel, J.-P., Ethé, C., Fairhead, L., Fichefet, T.,

1162 Flavoni, S., Friedlingstein, P., Grandpeix, J.-Y., Guez, L., Guilyardi, E., Hau all glustaine, D.,

1163 Hourdin, F., Idelkadi, A., Ghattas, J., Joussaume, S., Kageyama, M., Krinner, G., Labetoulle, S.,

1164 Lahellec, A., Lefebvre, M.-P., Lefevre, F., Levy, C., Li, Z. X., Lloyd, J., Lott, F., Madec, G., Mancip,

1165 M., Marchand, M., Masson, S., Meurdesoif, Y., Mignot, J., Musat, I., Parouty, S., Polcher, J., Rio, C.,

1166 Schulz, M., Swingedouw, D., Szopa, S., Talandier, C., Terray, P., Viovy, N. and Vuichard, N.:

1167 Climate Change Projections Using the IPSL-CM5 Earth System Model: From CMIP3 to CMIP5,

1168 Clim. Dynam., 40, 2123-2165, https://doi.org/10.1007/s00382-012-1636-1, 2013.

1169

1170 Durre I., Menne, M. J., Gleason, B. E., Houston, T. G. and Vose, R. S.: Comprehensive automated

1171 quality assurance of daily surface observations, J. Applied Meteor. and Climatol., 49, 1615-1633,

1172 doi.10.1175/2010JAMC2375.1, 2010.

1173

1174 Durre I., Menne, M. J. and Vose, R. S.: Strategies for evaluating quality assurance procedures, J.

1175 Applied Meteor. and Climatol., 47, 1785-1791, doi:10.1175/2007JAMC1706.1, 2008.

1176

1177 Eaton, B.: User's Guide to the Community Atmosphere Model CAM-CAM-5.1.1, NCAR

1178 (https://www.cesm.ucar.edu/models/cesm1.0/cam/docs/ug5_1_1/ug.html), Accessed 10/9/21, 2010.

1179

1180 Edwards, J. M. and Slingo, A.: Studies with a flexible new radiation code. I: Choosing a configuration

1181 for a large-scale model. Q.J.R. Meteorol. Soc., 122: 689-719. https://doi.org/10.1002/qj.49712253107,

1182 1996.

1183

1184 Eisawi, A. and Schrank, E.: Upper Cretaceous to Neogene palynology of the Melut Basin, southeast

1185 Sudan, Palynology, 32, 101-129, DOI: 10.1080/01916122.2008.9989653, 2008.

1186

1187 Emanuel, K. A.: A scheme for representing cumulus convection in large-scale models, J. Atmos. Sci.,

1188 48(21), 2313-2329, https://doi.org/10.1175/1520-0469(1991)0482.0.CO;2, 1991.

1189

1190 Eyring, V., Bony, S., Meehl, G. A., Senior, C. A., Stevens, B., Stouffer, R. J., and Taylor, K. E.:

1191 Overview of the Coupled Model Intercomparison Project Phase 6 (CMIP6) experimental design and

1192 organization, Geosci. Model Dev., 9, 1937-1958, doi:10.5194/gmd-9-1937-2016, 2016.

1193

1194 Farnsworth, A., Lunt, D. J., Robinson, S.A., Valdes, P.J., Roberts, W.H.G., Clift, P.D., Markwick, P.,

1195 Su, T., Wrobel, N., Bragg, F., Kelland, S.J. and Pancost, R.D.: Past East Asian monsoon evolution

1196 controlled by paleogeography, not CO2. Science Advances, 5, 10, DOI: 10.1126/sciadv.aax1697,

1197 2019.

1198

1199 Fouquart, Y. and Bonnel, B.: Computations of solar heating of the Earth's atmosphere: A new

1200 parameterization, Beitr. Phys. Atmos., 53, 35-62, 1980.

1201

1202 Funk, C., Nicholson, S., Landsfeld, M., Klotter, D., Peterson, P. and Harrison, L.: The Centennial

1203 Trends Greater Horn of Africa precipitation dataset, Sci Data 2, 150050,

1204 https://doi.org/10.1038/sdata.2015.50, 2015.

1205

1206 Galbraith, E. D., Kwon, E. Y., Gnanadesikan, A., Rodgers, K. B., Griffies, S. M., Bianchi, D.,

1207 Sarmiento, J. L., Dunne, J. P., Simeon, J., Slater, R. D., Wittenberg, A. T. and Held, I. M.: Climate

1208 Variability and Radiocarbon in the CM2Mc Earth System Model, J. Clim., 24, 4230-4254,

1209 https://doi.org/10.1175/2011JCLI3919.1, 2011.

1210

1211 Goha, R. B., Zeli, B. D., Konan, R. Y., Tea-Yassi, J., Kouadio, D. K. and Tahi, I.: Stratigraphie

1212 palynologique du Maastrichtien supérieur-Eocène supérieur du bassin sédimentaire offshore de Côte

1213 d'Ivoire, Afrique de l'ouest, International Journal of African Studies, 6, 40-57, 2016.

1214

1215 Grant, A.: Chapter 2 Understanding the Unified Model (Section 2.1.6), in Matthews, D.: Unified

1216 Model User Guide, http://www.ukscience.org/_Media/UM_User_Guide.pdf, Accessed 22/9/21, 1998.

1217

1218 Guo, C., Bentsen, M., Bethke, I., Ilicak, M., Tjiputra, J., Toniazzo, T., Schwinger, J. and Otterå, O.

1219 H.: Description and evaluation of NorESM1_F: a fast version of the Norwegian Earth System Model

1220 (NorESM), Geosci. Model Dev., 12, 343-362, https://doi.org/10.5194/gmd-12-343-2019, 2019.

1221

1222 Hack, J. J.: Parameterization of moist covection in the NCAR Community Climate Model CCM2, J.

1223 Geophys. Res. Atmos., 99(D3): 5551-5568, DOI:10.1029/93JD03478, 1994.

1224

1225 Hagemann, S.: An improved land surface parameter dataset for global and regional climate models,

1226 Max Planck Institute for Meteorology, Report No. 336,

1227 https://citeseerx.ist.psu.edu/viewdoc/download?doi=10.1.1.471.2882&rep=rep1&type=pdf, Accessed

1228 17/9/21, 2002.

1229

1230 Harrison, S. P. and Prentice, I. C.: Climate and CO_2 controls on global vegetation distribution at the

1231 last glacial maximum: analysis based on palaeovegetation data, biome modelling and palaeoclimate

1232 simulations, Glob. Change Bio., 9 (7), 983-1004, https://doi.org/10.1046/j.1365-2486.2003.00640.x,

1233 2003.

1234

1235 Harrison, S. P., Bartlein, P. J., Brewer, S., Prentice, I. C., Boyd, M., Hessler, I., Holmgren, K., Izumi,

1236 K. and Willis, K.: Climate model benchmarking with glacial and mid-Holocene climates, Clim. Dyn.,

1237 43, 671-688, https://doi.org/10.1007/s00382-013-1922-6, 2014.

1238

1239 Hasumi, H.: CCSR Ocean Component Model (COCO) Version 2.1, Technical Report, The University
1240 of Tokyo, Tokyo, Japan, 2000.

1241

1242 Haywood, A. M., Tindall, J. C., Dowsett, H. J., Dolan, A. M., Foley, K. M., Hunter, S. J., Hill, D. J.,
1243 Chan, W.-L., Abe-Ouchi, A., Stepanek, C., Lohmann, G., Chandan, D., Peltier, W. R., Tan, N.,
1244 Contoux, C., Ramstein, G., Li, X., Zhang, Z., Guo, C., Nisancioglu, K. H., Zhang, Q., Li, Q., Kamae,
1245 Y., Chandler, M. A., Sohl, L. E., Otto-Bliesner, B. L., Feng, R., Brady, E. C., von der Heydt, A. S.,
1246 Baatsen, M. L. J. and Lunt, D. J.: The Pliocene Model Intercomparison Project Phase 2: large-scale
1247 climate features and climate sensitivity, Clim. Past, 16, 2095-2123, https://doi.org/10.5194/cp-16-
1248 2095-2020, 2020.

1249

1250 Held, I. M. and Soden, B. J.: Robust Responses of the Hydrological Cycle to Global Warming, J.
1251 Clim., 19 (21), 5686-5699, DOI: https://doi.org/10.1175/JCLI3990.1, 2006.

1252

1253 Herold, N., Buzan, J., Seton, M., Goldner, A., Green, J. A. M., Müller, R. D., Markwick, P. and
1254 Huber, M.: A suite of early Eocene (~55 Ma) climate model boundary conditions, Geosci. Model
1255 Dev., 7, 2077-2090, doi:10.5194/gmd-7-2077-2014, 2014.

1256

1257 Hijmans, R. J., Cameron, S. E., Parra, J. L., Jones, P. G. and Jarvis, A.: Very high resolution
1258 interpolated climate surfaces for global land areas, Int. J. Clim., 25, 1965-1978,
1259 https://doi.org/10.1002/joc.1278, 2005.

1260

1261 Huber, M. and Caballero, R.: The early Eocene equable climate problem revisited, Clim. Past, 7, 603-
1262 633, doi:10.5194/cp-7-603-2011, 2011.

1263

1264 Hurrell, J. W., Holland, M. M., Gent, P. R., Ghan, S., Kay, J. E., Kushner, P. J., Lamarque, J. F.,
1265 Large, W. G., Lawrence, D., Lindsay, K., Lipscomb, W. H., Long, M. C., Mahowald, N., Marsh, D.
1266 R., Neale, R. B., Rasch, P., Vavrus, S., Vertenstein, M., Bader, D., Collins, W. D., Hack, J. J., Kiehl,
1267 J. T. and Marshall, S.: The community earth system model: A framework for collaborative research,
1268 B. Am. Meteorol. Soc., 94, 1339-1360, https://doi.org/10.1175/BAMS-D-12-00121.1, 2013.

1269

1270 Hutchinson, D. K., de Boer, A. M., Coxall, H. K., Caballero, R., Nilsson, J. and Baatsen, M.: Climate
1271 sensitivity and meridional overturning circulation in the late Eocene using GFDL CM2.1, Clim. Past,
1272 14, 789-810, https://doi.org/10.5194/cp-14-789-2018, 2018.

1273

1274 Hollis, C. J., Dunkley Jones, T., Anagnostou, E., Bijl, P. K., Cramwinckel, M. J., Cui, Y., Dickens, G.
1275 R., Edgar, K. M., Eley, Y., Evans, D., Foster, G. L., Frieling, J., Inglis, G. N., Kennedy, E. M.,

1276   Kozdon, R., Lauretano, V., Lear, C. H., Littler, K., Lourens, L., Meckler, A. N., Naafs, B. D. A.,

1277   Pälike, H., Pancost, R. D., Pearson, P. N., Röhl, U., Royer, D. L., Salzmann, U., Schubert, B. A.,

1278   Seebeck, H., Sluijs, A., Speijer, R. P., Stassen, P., Tierney, J., Tripati, A., Wade, B., Westerhold, T.,

1279   Witkowski, C., Zachos, J. C., Zhang, Y. G., Huber, H. and Lunt, D. J.: The DeepMIP contribution to

1280   PMIP4: methodologies for selection, compilation and analysis of latest Paleocene and early Eocene

1281   climate proxy data, incorporating version 0.1 of the DeepMIP database, Geosci. Model Dev., 12,

1282   3149–3206, https://doi.org/10.5194/gmd-12-3149-2019, 2019.

1283

1284   Holtslag, A. and Boville, B.: Local versus nonlocal boundary-layer diffusion in a global climate

1285   model, J. Clim., 6, 1825-1825, https://doi.org/10.1175/1520-

1286   0442(1993)006<1825:LVNBLD>2.0.CO;2, 1993.

1287

1288   Hyland, E., Sheldon, N. D. and Fan, M.: Terrestrial paleoenvironmental reconstructions indicate

1289   transient peak warming during the early Eocene climatic optimum, Geol. Soc. Am. Bull., 125(7-8),

1290   1338-1348, DOI:10.1130/B30761.1, 2013.

1291

1292   Inglis, G. N., Bragg, F., Burls, N. J., Cramwinckel, M. J., Evans, D., Foster, G. L., Huber, M., Lunt,

1293   D. J., Siler, N., Steinig, S., Tierney, J. E., Wilkinson, R., Anagnostou, E., de Boer, A. M., Dunkley

1294   Jones, T., Edgar, K. M., Hollis, C. J., Hutchinson, D. K., and Pancost, R. D.: Global mean surface

1295   temperature and climate sensitivity of the early Eocene Climatic Optimum (EECO), Paleocene–

1296   Eocene Thermal Maximum (PETM), and latest Paleocene, Clim. Past, 16, 1953-1968,

1297   https://doi.org/10.5194/cp-16-1953-2020, 2020.

1298

1299   IPCC: Climate Change 2013: The Physical Science Basis. Contribution of Working Group I to the

1300   Fifth Assessment Report of the Intergovernmental Panel on Climate Change [Stocker, T. F., D. Qin,

1301   G.-K. Plattner, M. Tignor, S. K. Allen, J. Boschung, A. Nauels, Y. Xia, V. Bex and P. M. Midgley

1302   (eds.)], Cambridge University Press, Cambridge, United Kingdom and New York, NY, USA, pp

1303   1535, https://www.ipcc.ch/report/ar5/wg1/, 2013.

1304

1305   IPCC: Climate Change 2021: The Physical Science Basis. Contribution of Working Group I to the

1306   Sixth Assessment Report of the Intergovernmental Panel on Climate Change [Masson-Delmotte, V.,

1307   P. Zhai, A. Pirani, S.L. et al. (eds.)], Cambridge University Press, Cambridge, United Kingdom,

1308   https://www.ipcc.ch/report/ar6/wg1/, 2021.

1309

1310   Jacobs, B. F. and Herendeen, P. S.: Eocene dry climate and woodland vegetation in tropical Africa

1311   reconstructed from fossil leaves from northern Tanzania, Palaeogeography, Palaeoclimatology,

1312   Palaeoecology, 213, 115-123, 10.1016/S0031-0182(04)00368-2, 2004.

1313

1314 Jungclaus, J. H., Keenlyside, N., Botzet, M., Haak, H., Luo, J.-J., Latif, M., Marotzke, J.,

1315 Mikolajewicz, U. and Roeckner, E.: Ocean circulation and tropical variability in the coupled model

1316 ECHAM5/MPI-OM, J. Climate, 19, 3952-3972, https://doi.org/10.1175/JCLI3827.1, 2006.

1317

1318 K-1 model developers: K-1 coupled model (MIROC) description, Technical Report, Center for

1319 Climate System Research (University of Tokyo), National Institute for Environmental Studies,

1320 Frontier Research Center for Global Change, Tokyo, Japan, 2004.

1321

1322 Kageyama, M., Braconnot, P., Harrison, S. P., Haywood, A. M., Jungclaus, J. H., Otto-Bliesner, B. L.,

1323 Peterschmitt, J.-Y., Abe-Ouchi, A., Albani, S., Bartlein, P. J., Brierley, C., Crucifix, M., Dolan, A.,

1324 Fernandez-Donado, L., Fischer, H., Hopcroft, P. O., Ivanovic, R. F., Lambert, F., Lunt, D. J.,

1325 Mahowald, N. M., Peltier, W. R., Phipps, S. J., Roche, D. M., Schmidt, G. A., Tarasov, L., Valdes, P.

1326 J., Zhang, Q. and Zhou, T.: The PMIP4 contribution to CMIP6 – Part 1: Overview and over-arching

1327 analysis plan, Geosci. Model Dev., 11, 1033–1057, https://doi.org/10.5194/gmd-11-1033-2018, 2018.

1328

1329 Kaiser, T. M. Ansorge, J., Arratia, G., Bullwinkel, V., Gunnell, G. F., Herendeen, P. S., Jacobs, B.,

1330 Mingram, J., Msuya, C., Musolff, A., Naumann, R., Schulz, E. and Wilde, V.: The maar lake of

1331 Mahenge (Tanzania) unique evidence of Eocene terrestrial environments in sub-Sahara Africa,

1332 Zeitschrift der Deutschen Gesellschaft für Geowissenschaften Band 157 Heft 3, DOI: 10.1127/1860-

1333 1804/2006/0157-0411, 2006.

1334

1335 Kaplan, J. O., Bigelow, N. H., Prentice, I. C., Harrison, S. P., Bartlein, P. J., Christensen, T. R.,

1336 Cramer, W., Matveyeva, N. V., McGuire, A. D., Murray, D. F., Razzhivin, V. Y., Smith, B., Walker,

1337 D. A., Anderson, P. M., Andreev, A. A., Brubaker, L. B., Edwards, M. E. and Lozhkin, A. V.:

1338 Climate change and Arctic ecosystems: 2. Modeling, paleodata-model comparisons, and future

1339 projections, J. Geophys. Res., 108, 8171, doi:10.1029/2002jd002559, 2003.

1340

1341 Keery, J. S., Holden, P. B. and Edwards, N. R.: Sensitivity of the Eocene climate to CO2 and orbital

1342 variability, Clim. Past, 14, 215-238, DOI: 10.5194/cp-14-215-2018, 2018

1343

1344 Kennedy-Asser, A. T., Lunt, D. J., Farnsworth, A. and Valdes, P. J.: Assessing mechanisms and

1345 uncertainty in modeled climatic change at the Eocene-Oligocene transition, Paleoceanography and

1346 Paleoclimatology, 34, 16-34. https://doi.org/10.1029/2018PA003380, 2019.

1347

1348 Laval, K., Sadourny, R. and Serafini, Y.: Land surface processes in a simplified general circulation

1349 model, Geophys. Astrophys. Fluid Dyn., 17(1), 129-150,

1350 https://doi.org/10.1080/03091928108243677, 1981.

1351

1352 A. N., Quade, J., Dupont-Nivet, G.and Jaeger, J. J.: Asian monsoons in a late Eocene greenhouse

1353 world, Nature, 513, 7519, DOI: 10.1038/nature13704, 2014

1354

1355 Li, X., Guo, C., Zhang, Z., Otterå, O. H. and Zhang, R.: PlioMIP2 simulations with NorESM-L and

1356 NorESM1-F, Clim. Past, 16, 183-197, https://doi.org/10.5194/cp-16-183-2020, 2020.

1357

1358 Liu, W., Xie, S.-P., Liu, Z. and Zhu, J.: Overlooked possibility of a collapsed Atlantic Meridional

1359 Overturning Circulation in warming climate, Science Advances, 3(1), e1601666.

1360 https://doi.org/10.1126/sciadv.1601666, 2017.

1361

1362 Liu, X. D., Dong, B. W., Yin, Z. Y., Smith, R. S. and Guo, Q. C.: Continental drift, plateau uplift, and

1363 the evolutions of monsoon and arid regions in Asia, Africa, and Australia during the Cenozoic,

1364 Science China-Earth Sciences, 62, 1053-1075, DOI: 10.1007/s11430-018-9337-8, 2019.

1365

1366 Lott, F.: Alleviation of stationary biases in a GCM through a mountain drag parameterization scheme

1367 and a simple representation of mountain lift forces, Mon. Wea. Rev., 127(5), 788-801,

1368 https://doi.org/10.1175/1520-0493(1999)127<0788:AOSBIA>2.0.CO;2, 1999.

1369

1370 Louis, J. F.: A parametric model of vertical eddy fluxes in the atmosphere, Boundary-Layer

1371 Meteorol., 17(2), 187-202, https://doi.org/10.1007/BF00117978, 1979.

1372

1373 Lunt, D. J., Bragg, F., Chan, W.-L., Hutchinson, D. K., Ladant, J.-B., Morozova, P., Niezgodzki, I.,

1374 Steinig, S., Zhang, Z., Zhu, J., Abe-Ouchi, A., Anagnostou, E., de Boer, A. M., Coxall, H. K.,

1375 Donnadieu, Y., Foster, G., Inglis, G. N., Knorr, G., Langebroek, P. M., Lear, C. H., Lohmann, G.,

1376 Poulsen, C. J., Sepulchre, P., Tierney, J. E., Valdes, P. J., Volodin, E. M., Dunkley Jones, T., Hollis,

1377 C. J., Huber, M. and Otto-Bliesner, B. L.: DeepMIP: model intercomparison of early Eocene climatic

1378 optimum (EECO) large-scale climate features and comparison with proxy data, Clim. Past, 17, 203-

1379 227, https://doi.org/10.5194/cp-17-203-2021, 2021.

1380

1381 Lunt, D. J., Dunkley Jones, T., Heinemann, M., Huber, M., LeGrande, A., Winguth, A., Loptson, C.,

1382 Marotzke, J., Roberts, C. D., Tindall, J., Valdes, P. and Winguth, C.: A model-data comparison for a

1383 multi-model ensemble of early Eocene atmosphere-ocean simulations: EoMIP, Clim. Past, 8, 1717-

1384 1736, https://doi.org/10.5194/cp-8-1717-2012, 2012.

1385

1386 Lunt, D. J., Huber, M., Anagnostou, E., Baatsen, M. L. J., Caballero, R., DeConto, R., Dijkstra, H. A.,

1387 Donnadieu, Y., Evans, D., Feng, R., Foster, G. L., Gasson, E., von der Heydt, A. S., Hollis, C. J.,

1388 Inglis, G. N., Jones, S. M., Kiehl, J., Kirtland Turner, S., Korty, R. L., Kozdon, R., Krishnan, S.,

1389 Ladant, J.-B., Langebroek, P., Lear, C. H., LeGrande, A. N., Littler, K., Markwick, P., Otto-Bliesner,

1390 B., Pearson, P., Poulsen, C. J., Salzmann, U., Shields, C., Snell, K., Stärz, M., Super, J., Tabor, C.,

1391 Tierney, J. E., Tourte, G. J. L., Tripati, A., Upchurch, G. R., Wade, B. S., Wing, S. L., Winguth, A.

1392 M. E., Wright, N. M., Zachos, J. C. and Zeebe, R. E.: The DeepMIP contribution to PMIP4:

1393 experimental design for model simulations of the EECO, PETM, and pre-PETM (version 1.0),

1394 Geosci. Model Dev., 10, 889-901, https://doi.org/10.5194/gmd-10-889-2017, 2017.

1395

1396 Ma, Y. Q., Fan, M. J., Lu, Y. C., Liu, H. M., Zhang, S. P. and Liu, X. F.: Stable isotope record of

1397 middle Eocene summer monsoon and its instability in eastern China, Global and Planetary Change,

1398 175, 103-112, DOI: 10.1016/j.gloplacha.2019.02.007, 2019.

1399

1400 Maidment, R. I., Grimes, D., Black, E., Tarnavsky, E., Young, M., Greatrex, H., Allan, R. P., Stein,

1401 T., Nkonde, E., Senkunda, S. and Alcántara, E. M. U.: A new, long-term daily satellite-based rainfall

1402 dataset for operational monitoring in Africa, nature Scientific Data, 4: 170063. DOI:

1403 10.1038/sdata.2017.63, 2017.

1404

1405 Maidment, R. I., Grimes, D., Allan, R. P., Tarnavsky, E., Stringer, M., Hewison, T., Roebeling, R.

1406 and Black, E.: The 30-year TAMSAT African Rainfall Climatology and Time-series (TARCAT) Data

1407 Set, J. Geophys. Res.: Atmos., 119(10): 619-610, 644. DOI: 10.1002/2014JD021927, 2014.

1408

1409 Marsland, S. J., Haak, H., Jungclaus, J. H., Latif, M. and Roske, F.: The Max-Planck-Institute global

1410 ocean/sea ice model with orthogonal curvilinear coordinates, Ocean Model., 5, 91-127,

1411 https://doi.org/10.1016/S1463-5003(02)00015-X, 2003.

1412

1413 Martínez-Botí, M. A., Foster, G. L., Chalk, T. B., Rohling, E. J., Sexton, P. F., Lunt, D. J., Pancost, R.

1414 D., Badger, M. P. S. and Schmidt, D. N.: Plio-Pleistocene climate sensitivity evaluated using high-

1415 resolution CO_2 records, Nature, 518, 49-54, https://doi.org/10.1038/nature14145, 2015.

1416

1417 Menne, M. J., Durre I., Vose, R. S., Gleason, B. E. and Houston, T. G.: An overview of the Global

1418 Historical Climatology Network-Daily Database, J. Atmos. and Oceanic Tech., 29, 897-910,

1419 doi.10.1175/JTECH-D-11-00103.1, 2012.

1420

1421 Monerie, P-A., Wainwright, C. M. and Sidibe, M.: Model uncertainties in climate change impacts on

1422 Sahel precipitation in ensembles of CMIP5 and CMIP6 simulations, Clim. Dyn., 55, 1385-1401,

1423 https://doi.org/10.1007/s00382-020-05332-0, 2020.

1424

1425 Moorthi, S. and Suarez, M. J.: Relaxed Arakawa-Schubert. A Parameterization of Moist Convection

1426 for General Circulation Models, Mon. Weather Rev., 120, 978-1002, https://doi.org/10.1175/1520-

1427 0493(1992)120<0978:RASAPO>2.0.CO;2, 1992.

1428

1429 Morcrette, J. J., Smith, L. and Fouquart, Y.: Pressure and temperature dependence of the absorption

1430 in longwave radiation parameterizations, Beitr. Phys. Atmos., 59, 455-469, ISSN 0005-8173, 1986.

1431

1432 Morrison, H. and Gettelman, A.: A New Two-Moment Bulk Stratiform Cloud Microphysics Scheme

1433 in the Community Atmosphere Model, Version 3 (CAM3). Part I: Description and Numerical Tests, J.

1434 Clim., 21(15), 3642-3659, DOI:10.1175/2008JCLI2105.1, 2008.

1435

1436 Naafs, B. D. A., Rohrssen, M., Inglis, G. N., Lähteenoja, O., Feakins, S. J., Collinson, M. E.,

1437 Kennedy, E. M., Singh, P. K., Singh, M. P., Lunt, D. J. and Pancost, R. D.: High temperatures in the

1438 terrestrial mid-latitudes during the early Palaeogene, Nature Geosci 11, 766-771,

1439 https://doi.org/10.1038/s41561-018-0199-0, 2018.

1440

1441 Neale, R. B., Richter, J. H. and Jochum M.: The impact of convection on ENSO: From a delayed

1442 oscillator to a series of events, J. Clim., 21(22), 5904-5924, https://doi.org/10.1175/2008JCLI2244.1,

1443 2008.

1444

1445 Neale, R. B., Richter, J. H., Park, S., Lauritzen, P. H., Vavrus, S. J., Rasch, P. J. and Zhang, M.: The

1446 Mean Climate of the Community Atmosphere Model (CAM4) in Forced SST and Fully Coupled

1447 Experiments, J. Clim., 26(14), 5150-5168, https://doi.org/10.1175/JCLI-D-12-00236.1, 2013.

1448

1449 Okeke, K. K. and Umeji, O. P.: Palynostratigraphy, palynofacies and palaeoenvironment of deposition

1450 of Selandian to Aquitanian sediments, southeastern Nigeria, Journal of African Earth Sciences, 120,

1451 102-124, DOI: 10.1016/j.jafrearsci.2016.04.020, 2016

1452

1453 Park, S. and Bretherton, C. S.: The University of Washington Shallow Convection and Moist

1454 Turbulence Schemes and Their Impact on Climate Simulations with the Community Atmosphere

1455 Model, J. Clim., 22(12), 3449-3469, DOI:10.1175/2008JCLI2557.1, 2009.

1456

1457　Pearson, P. N., Ditchfield, P. W., Singano, J., Harcourt-Brown, K. G., Nicholas, C. J. and Olsson, R.

1458　K.: Warm tropical sea surface temperatures in the Late Cretaceous and Eocene epochs, Nature, 413,

1459　481-487, DOI: 10.1038/35097000, 2001.

1460

1461　Pearson, P. N. and Wade, B. S.: Stable warm tropical climate through the Eocene Epoch, Geology, 35

1462　(1), https://doi.org/10.1130/G24462Y.1, 2007.

1463

1464　Quan, C., Liu, Y. S. and Utescher, T.: Eocene monsoon prevalence over China: A paleobotanical

1465　perspective, Palaeogeography Palaeoclimatology Palaeoecology, 365, 302-311, DOI:

1466　10.1016/j.palaeo.2012.09.035, 2012.

1467

1468　Rae, J. W. B., Zhang, Y. G., Liu, X., Foster, G. L., Stoll, H. M. and Whiteford, R. D. M.: Atmospheric

1469　CO_2 over the past 66 million years from marine archives, Annual Review of Earth and Planetary

1470　Sciences, 49, 606-641, https://doi.org/10.1146/annurev-earth-082420-063026, 2021.

1471

1472　Rasch, P. J. and Kristjánsson, J. E.: A comparison of the CCM3 model climate using diagnosed and

1473　predicted condensate parameterizations, J. Clim., 11(7), 1587-1614, https://doi.org/10.1175/1520-

1474　0442(1998)011<1587:ACOTCM>2.0.CO;2, 1998.

1475

1476　Reichgelt, T., D'Andrea, W. J. and Fox, B. R. S.: Abrupt plant physiological changes in southern New

1477　Zealand at the termination of the Mi-1 event reflect shifts in hydroclimate and pCO_2, EPSL, 455, 115–

1478　124, https://doi.org/10.1016/j.epsl.2016.09.026, 2016.

1479

1480　Reichgelt, T., Greenwood, D. R., Steinig, S., Conran, J. G., Scriven, L. J., Zhu, J., Hutchinson, D. K.

1481　and Lunt, D. J.: Plant proxy evidence for high rainfall and productivity in the Eocene of Australia,

1482　Clim. Past, in Prep.

1483

1484　Richter, J. H. and Rasch, P. J.: Effects of convective momentum transport on the atmospheric

1485　circulation in the Community Atmosphere Model, version 3, J. Clim., 21, 1487-1499,

1486　https://doi.org/10.1175/2007JCLI1789.1, 2008.

1487

1488　Roeckner, E., Bäuml, G., Bonaventura, L., Brokopf, R., Esch, M., Giorgetta, M., Hagemann, S.,

1489　Kirchner, I., Kornbleuh, L., Manzini, E., Rhodin, A., Schlese, U., Schulzweida, U. and Tompkins, A.:

1490　The atmospheric general circulation model ECHAM 5. PART I: Model description, Report 349, Max-

1491　Planck Institut für Meteorologie, Hamburg, Germany, 140 pp., 2003.

1492

1493   Rotstayn, L. D.: A physically based scheme for the treatment of stratiform clouds and precipitation in

1494   large-scale models. I: Description and evaluation of the microphysical processes, Q. J. R. Meteorol.

1495   Soc., 123, 1227–1282, https://doi.org/https://doi.org/10.1002/qj.49712354106, 1997.

1496

1497   Rougier, J. C., Goldstein, M. and House, L.: Second-order exchangeability analysis for multi-model

1498   ensembles, Journal of the American Statistical Association, 108, 852-863,

1499   doi:10.1080/01621459.2013.802963, 2013.

1500

1501   Salami, M. B.: Late Cretaceous and Early Tertiary Palynofacies of Southwestern Nigeria, Revista

1502   Espanola de Micropaleontologia, XVI, 415-423, 1984.

1503

1504   Salard-Cheboldaeff, M.: Palynologie Maestrichtienne et Tertiaire du Cameroun. Etude qualitative et

1505   repartition verticale des principales especes, Review of Palaeobotany and Palynology, 28, 365-388,

1506   https://doi.org/10.1016/0034-6667(79)90032-0, 1979.

1507

1508   Salerno, J., Diem, J. E., Konecky, B. L. and Hartter, J.: Recent intensification of the seasonal rainfall

1509   3391 cycle in equatorial Africa revealed by farmer perceptions, satellite-based estimates, and ground-

1510   based station 3392 measurements, Climatic Change, 153(1-2):123-139, DOI:10.1007/s10584-019-

1511   02370-4, 2019.

1512

1513   Sepulchre, P., Caubel, A., Ladant, J.-B., Bopp, L., Boucher, O., Braconnot, P., Brockmann, P., Cozic,

1514   A., Donnadieu, Y., Dufresne, J.-L., Estella-Perez, V., Ethé, C., Fluteau, F., Foujols, M.-A., Gastineau,

1515   G., Ghattas, J., Hauglustaine, D., Hourdin, F., Kageyama, M., Khodri, M., Marti, O., Meurdesoif, Y.,

1516   Mignot, J., Sarr, A.-C., Servonnat, J., Swingedouw, D., Szopa, S. and Tardif, D.: IPSL-CM5A2 – an

1517   Earth system model designed for multi-millennial climate simulations, Geosci. Model Dev., 13, 3011-

1518   3053, https://doi.org/10.5194/gmd-13-3011-2020, 2020.

1519

1520   Smagorinsky, J.: General Circulation Experiments with the Primitive Equations: I The Basic

1521   Experiment, Mon. Weather Rev., 91, 99-164, https://doi.org/10.1175/1520-

1522   0493(1963)091<0099:GCEWTP>2.3.CO;2, 1963.

1523

1524   Stepanek, C. and Lohmann, G.: Modelling mid-Pliocene climate with COSMOS, Geosci. Model Dev.,

1525   5, 1221-1243, https://doi.org/10.5194/gmd-5-1221-2012, 2012.

1526

1527   Takata, K., Watanabe, T. and Emori, S.: Development of the minimal advanced treatments of surface

1528   interaction and runoff, Global Planet. Change, 38, 209-222, doi:10.1016/S0921-8181(03)00030-4,

1529   2003.

1530

1531 Tarnavsky, E., Grimes, D., Maidment, R. I., Black, E., Allan, R. P., Stringer, M., Chadwick, R. and

1532 Kayitakire, F.: Extension of the TAMSAT Satellite-based Rainfall Monitoring over Africa and from

1533 1983 to present. J. Applied Meteor. and Climatol., 53(12): 2805-2822. DOI: 10.1175/JAMC-D-14-

1534 0016.1, 2014.

1535

1536 Taylor, K. E., Stouffer, R. J. and Meehl, G. A.: An overview of CMIP5 and the experiment design, B.

1537 Am. Meteorol. Soc, 93, 485-498, https://doi.org/10.1175/BAMS-D-11-00094.1, 2011.

1538

1539 Tiedtke, M.: Representation of Clouds in Large-Scale Models, Mon. Weather Rev., 121, 3040-3061,

1540 https://doi.org/10.1175/1520-0493(1993)121<3040:ROCILS>2.0.CO;2, 1993.

1541

1542 Tierney, J. E., Poulsen, C. J., Montañez, I. P., Bhattacharya, T., Feng, R., Ford, H. L., Hönisch, B.,

1543 Inglis, G. N., Petersen, S. V., Sagoo, N., Tabor, C. R., Thirumalai, K., Zhu, J., Burls, N. J., Foster, G.

1544 L., Goddéris, Y., Huber, B. T., Ivany, L. C., Turner, S. K., Lunt, D. J., McElwain, J. C., Mills, B. J.

1545 W., Otto-Bliesner, B. L., Ridgwell, A. and Zhang, Y-G.: Past climates inform our future, Science,

1546 370 (6510), DOI: 10.1126/science.aay3701, 2020.

1547

1548 Tokioka, T., Yamazaki, K., Kitoh, A. and Ose, T.: The Equatorial 30-60 day Oscillation and the

1549 Arakawa-Schubert Penetrative Cumulus Parameterization, J. Meteorol. Soc. Japan, 66, 883-901,

1550 https://doi.org/10.2151/jmsj1965.66.6_883, 1988.

1551

1552 Utescher, T., Bruch, A. A., Erdei, B., François, L., Ivanov, D., Jacques, F. M. B., Kern, A. K., Liu,

1553 Y.-S., Mosbrugger, V. and Spicer, R. A.: The Coexistence Approach - Theoretical background and

1554 practical considerations of using plant fossils for climate quantification, Palaeogeography,

1555 Palaeoclimatology, Palaeoecology, 410, 58-73, https://doi.org/10.1016/j.palaeo.2014.05.031, 2014.

1556

1557 Uzodimma, D. E.: Palynostratigraphy, Age Determination and Depositional Environments of the Imo

1558 Shale Exposures at the Okigwe/Port Harcourt Express Road Junction Okigwe, Southeastern Nigeria,

1559 Greener Journal of Physical Sciences, 3, 255-272, ISSN: 2276-7851, 2013.

1560

1561 van Dijk, J., Fernandez, A., Bernasconi, S. M., Caves Rugenstein, J. K., Passey, S. R. and White, T.:

1562 Spatial pattern of super-greenhouse warmth controlled by elevated specific humidity, Nat. Geosci.,

1563 13, 739–744, https://doi.org/10.1038/s41561-020-00648-2, 2020.

1564

1565 Valdes, P. J., Armstrong, E., Badger, M. P. S., Bradshaw, C. D., Bragg, F., Crucifix, M., Davies-

1566 Barnard, T., Day, J. J., Farnsworth, A., Gordon, C., Hopcroft, P. O., Kennedy, A. T., Lord, N. S.,

1567 Lunt, D. J., Marzocchi, A., Parry, L. M., Pope, V., Roberts, W. H. G., Stone, E. J., Tourte, G. J. L. and

1568 Williams, J. H. T.: The BRIDGE HadCM3 family of climate models: HadCM3@Bristol v1.0, Geosci.

1569 Model Dev., 10, 3715-3743, https://doi.org/10.5194/gmd-10-3715-2017, 2017.

1570

1571 Volodin, E. M. and Lykossov, V. N.: Parameterization of Heat and Moisture Transfer in the Soil-

1572 Vegetation System for Use in Atmospheric General Circulation Models: 2. Numerical Experiments in

1573 Climate Modeling, Izvestiya Atmospheric and Oceanic Physics, 34(5), 559-569, 1998.

1574

1575 Volodin, E. M., Mortikov, E. V., Kostrykin, S. V., Galin, V. Y., Lykossov, V. N., Gritsun, A. S.,

1576 Diansky, N. A., Gusev, A. V. and Iakovlev, N. G.: Simulation of the present-day climate with the

1577 climate model INMCM5, Clim. Dynam., 49, 3715-3734, 10.1007/s00382-017-3539-7, 2017.

1578

1579 Volodin, E. M., Mortikov, E. V., Kostrykin, S. V., Galin, V. Y., Lykossov, V. N., Gritsun, A. S.,

1580 Diansky, N. A., Gusev, A. V., Iakovlev, N. G., Shestakova, A. A. and Emelina, S. V.: Simulation of

1581 the modern climate using the INMCM48 climate model, Russ. J. Numer. Anal. M., 33, 367-374,

1582 https://doi.org/10.1515/rnam-2018-0032, 2018.

1583

1584 West, C. K., Greenwood, D. R., Reichgelt, T., Lowe, A. J., Vachon, J. M., and Basinger, J. F.:

1585 Paleobotanical proxies for early Eocene climates and ecosystems in northern North America from

1586 middle to high latitudes, Clim. Past, 16, 1387-1410, https://doi.org/10.5194/cp-16-1387-2020, 2020.

1587

1588 Westerhold, T., Marwan, N., Drury, A. J., Liebrand, D., Agnini, C., Anagnostou, E., Barnet, J. S. K.,

1589 Bohaty, S. M., De Vleeschouwer, D., Florindo, F., Frederichs, T., Hodell, D. A., Holbourn, A. E.,

1590 Kroon, D., Lauretano, V., Littler, K., Lourens, L. J., Lyle, M., Pälike, H., Röhl, U., Tian, J., Wilkens,

1591 R. H., Wilson, P. A. and Zachos, J. C.: An astronomically dated record of Earth's climate and its

1592 predictability over the last 66 million years, Science, 369(6509), 1383-1387,

1593 https://doi.org/10.1126/science.aba6853, 2020.

1594

1595 Wilf, P., Wing, S. L., Greenwood, D. R. and Greenwood, C. L.: Using fossil leaves as

1596 paleoprecipitation indicators: An Eocene example, Geology, 26, 203-206,

1597 https://doi.org/10.1130/0091-7613(1998)026<0203:UFLAPI>2.3.CO;2, 1998.

1598

1599 Williams, C. J. R., Guarino, M.-V., Capron, E., Malmierca-Vallet, I., Singarayer, J. S., Sime, L. C.,

1600 Lunt, D. J. and Valdes, P. J.: CMIP6/PMIP4 simulations of the mid-Holocene and Last Interglacial

1601 using HadGEM3: comparison to the pre-industrial era, previous model versions and proxy data, Clim.

1602 Past, 16, 1429-1450, https://doi.org/10.5194/cp-16-1429-2020, 2020.

1603

1604   Williams, C. J. R. and Kniveton, D. R. (eds). African Climate and Climate Change: Physical, Social

1605   and Political Perspectives. Springer Science+Business Media BV 2011. Dordrecht, Heidelberg,

1606   London and New York: 212pp. DOI: 10.1007/978-90-481-3842-5, 2011.

1607

1608   Williams, C. J. R., Kniveton, D. R. and Layberry, R.: Climatic and oceanic associations with daily

1609   rainfall extremes over southern Africa, Int. J. Clim., 27 (1): 93-108, https://doi.org/10.1002/joc.1376,

1610   2007.

1611

1612   Williams, C. J. R., Kniveton, D. R. and Layberry, R.: Influence of South Atlantic sea surface

1613   temperatures on rainfall variability and extremes over southern Africa, J. Clim., 21: 6498-6520, DOI:

1614   https://doi.org/10.1175/2008JCLI2234.1, 2008.

1615

1616   Williams, C. J. R., Kniveton, D. R. and Layberry, R.: Assessment of a climate model to reproduce

1617   rainfall variability and extremes over southern Africa, Theor. Applied Climatol., 99: 9-27, DOI:

1618   10.1007/s00704-009-0124-y, 2010.

1619

1620   Williams, C. J. R., Sellar, A. A., Ren, X., Haywood, A. M., Hopcroft, P., Hunter, S. J., Roberts, W. H.

1621   G., Smith, R. S., Stone, E. J., Tindall, J. C., and Lunt, D. J.: Simulation of the mid-Pliocene Warm

1622   Period using HadGEM3: experimental design and results from model–model and model–data

1623   comparison, Clim. Past, 17, 2139-2163, https://doi.org/10.5194/cp-17-2139-2021, 2021.

1624

1625   Willard, D. A., Donders, T. H., Reichgelt, T., Greenwood, D. R., Sangiorgi, F., Peterse, F., Nierop, K.

1626   G. J., Frieling, J., Schouten, S. and Sluijs, A.: Arctic vegetation, temperature, and hydrology during

1627   Early Eocene transient global warming events, Global and Planetary Change, 178, 139-152,

1628   https://doi.org/10.1016/j.gloplacha.2019.04.012, 2019.

1629

1630   Wright, I. J., Dong, N., Maire, V., Prentice, I. C., Westoby, M., Díaz, S., Gallagher, R. V., Jacobs, B.

1631   F., Kooyman, R., Law, E. A., Leishman, M. R., Niinemets, U., Reich, P. B., Sack, L., Villar, R.,

1632   Wang, H. and Wilf, P.: Global climatic drivers of leaf size, Science, 357(6354), 917–921, DOI:

1633   10.1126/science.aal4760, 2017.

1634

1635   Xie, Y. L., Wu, F. L. and Fang, X. M.: Middle Eocene East Asian monsoon prevalence over southern

1636   China: Evidence from palynological records, Global and Planetary Change, 175, 13-26, DOI:

1637   10.1016/j.gloplacha.2019.01.019, 2019.

1638

1639 Zhang, G. J. and McFarlane, N. A.: Sensitivity of climate simulations to the parameterization of

1640 cumulus convection in the Canadian Climate Centre general circulation model, Atmosphere–Ocean,

1641 33(3), 407-446, https://doi.org/10.1080/07055900.1995.9649539, 1995.

1642

1643 Zhang, M., Lin, W., Bretherton, C. S., Hack, J. J. and Rasch, P. J.: A modified formulation of

1644 fractional stratiform condensation rate in the NCAR Community Atmospheric Model (CAM2), J.

1645 Geophys. Res., 108(D1), 4035, https://doi.org/10.1029/2002JD002523, 2003.

1646

1647 Zhu, J., Poulsen, C. J. and Otto-Bliesner, B. L.: High climate sensitivity in CMIP6 model not

1648 supported by paleoclimate, Nat. Clim. Chang, 10, 378-379, https://doi.org/10.1038/s41558-020-0764-

1649 6, 2020.

1650

1651

1652